Optical properties of nanostructures from time-dependent density functional theory

Alberto Castro
Departamento de Física Teórica, Universidad de Valladolid,
E-47011 Valladolid (Spain) and Donostia International Physics Center (DIPC), 20018 San Sebastián (Spain)[*]

Miguel A.L. Marques
Institut für Theoretische Physik, Freie Universität Berlin, D-14175 Berlin (Germany)[†]

Julio A. Alonso
Departamento de Física Teórica, Universidad de Valladolid,
47011 Valladolid (Spain) and Donostia International Physics Center (DIPC), 20018 San Sebastián (Spain)[‡]

Angel Rubio
Dpto. Fisica de Materiales, Facultad de Químicas, Universidad del País Vasco,
Centro Mixto CSIC-UPV/EHU and Donostia International Physics Center (DIPC) Apdo. 1072, 20018 San Sebastian/Donostia, (Spain) [§]

(Dated: March 25, 2004)

We review the time-dependent density functional theory (TDDFT) and its use to investigate excited states of nanostructures. These excited states are routinely probed using electromagnetic fields. In this case, two different regimes are usually distinguished: i) If the electromagnetic field is "weak" – as in optical absorption of light – it is sufficient to treat the field within linear response theory; ii) Otherwise, nonlinear effects are important, and one has to resort to the full solution of the time-dependent Kohn-Sham equations. This latter regime is of paramount relevance in the emerging field of research with intense and ultrashort laser pulses. This review is divided in two parts: First we give a brief overview of the theoretical foundations of the theory, both in the linear and non-linear regimes, with special emphasis on the problem of the choice of the exchange-correlation functional. Then we present a sample of applications of TDDFT to systems ranging from atoms to clusters and to large biomolecules. Although, most of these applications are in the linear regime, we show a few examples of non-linear phenomena, such as the photo-induced dissociation of molecules. Many of these applications have been performed with the recently developed code `octopus` (`http://www.tddft.org/programs/octopus`).

Keywords: linear response, optical response, clusters, nonlinear processes, TDDFT, non-adiabatic molecular dynamics, high harmonic generation

Contents

I. INTRODUCTION

Nanostructures, including clusters, biomolecules and molecular-nanodevices, are nowadays at the heart of many fundamental and technological research projects. Characterization of their electronic, structural, and bonding properties is a real necessity. Optical, electron and time-resolved spectroscopies offer this possibility, allowing the study of static and dynamic electron-electron correlations. The electronic properties are sensitive to the evolution of the energy levels as the number of atoms in the cluster increases. The optical spectrum provides information on the electronic structure. In par-

ticular, the optical response of the clusters depends on their size and also on the cluster structure. This is an important feature, since the determination of the structure is, in general, a hard task, either for experimental techniques or for sophisticated total energy calculations, and knowledge of the geometrical structure of a cluster is required as a basis for understanding many of its properties.

This article is divided in two main parts: In section II we briefly review the theory of time-dependent density functional theory (TDDFT),[1–4] and the basic framework for the calculation of optical spectra of clusters and nanostructures. For a deeper study of the theoretical foundations and limitations we refer the reader to the available excellent reviews, namely Refs. [1,2] for the basics of TDDFT, and Ref. [4] for a detailed comparison of TDDFT with approaches based on many-body perturbation theory – including applications to nanostructures and solid-state systems. We have recently implemented this framework in the first principles code `octopus`,[5] that allows the study electron-ion dynamics of many-electron systems under the presence of arbitrary external electromagnetic fields. Section III is devoted to the applications of TDDFT, both in the linear and non-linear regimes, some of them performed with `octopus`. Contact with experiments and other works and techniques will be made all throughout the present paper.

A. Relation between theory and experiment

When a nanostructure interacts with an applied time-dependent electric field characterized by an external potential $v_{\rm ext}(\mathbf{r},\omega)$ the external field induces a time-dependent perturbation of the electron density $\delta n(\mathbf{r},\omega)$. We work in the longitudinal gauge, and neglect magnetic and current-induced effects. In the linear response regime, the dynamical susceptibility $\chi(\mathbf{r},\mathbf{r}',\omega)$ is given by

$$\delta n(\mathbf{r},\omega) = \int \mathrm{d}^3 r' \chi(\mathbf{r},\mathbf{r}',\omega) v_{\rm ext}(\mathbf{r}',\omega)\,. \tag{1.1}$$

From the value of $\delta n(\mathbf{r},\omega)$, it is straightforward to calculate the induced dipole moment (in the case of a dipolar field). The dynamical polarizability $\alpha(\omega)$, which is the ratio between the induced dipole moment and the magnitude of the applied electric field E_0, then becomes

$$\alpha(\omega) = \frac{e}{E_0}\int \mathrm{d}^3 r\, v_{\rm ext}(\mathbf{r})\delta n(\mathbf{r},\omega)\,. \tag{1.2}$$

Absorption of light can be viewed as a dissipation process induced by the electronic excitations: $\delta n(\mathbf{r},\omega)$ develops an imaginary part that represents the power absorption of the cluster. By application of Fermi's Golden Rule, one obtains the photoabsorption cross section:

$$\sigma(\omega) = \frac{4\pi\omega}{c}\Im\alpha(\omega)\,, \tag{1.3}$$

where $\Im\alpha(\omega)$ is the imaginary part of the dynamical polarizability and c is the velocity of light. The integral of the photoabsorption cross section leads to the dipole sum rule (or Thomas-Reiche-Kuhn sum rule)

$$\int_0^\infty \mathrm{d}\omega\,\sigma(\omega) = \frac{2\pi^2 e^2}{mc} Z\,, \tag{1.4}$$

where m is the electronic mass, Z is the total number of electrons taking part in the collective motion. Another widely used quantity is the strength function $S(\omega)$, which is connected to $\alpha(\omega)$ by

$$S(\omega) = \frac{2m}{\hbar^2}\sum_n \delta(\omega-\omega_n)\left|\langle n|\hat{Q}|0\rangle\right|^2 = \frac{2m\Im\alpha(\omega)}{\pi\hbar^2}\,. \tag{1.5}$$

The sum (an integral in the case of a continuum spectrum) extends over all the excited "many-body" states of the system $|n\rangle$. Furthermore, $|0\rangle$ denotes the ground state, ω_n are the excitation frequencies, and the operator $\hat{Q}$ represents the external field acting on the system (in what follows we will concentrate on dipolar excitations). Note that this is not the usual definition of the strength function given, for example, in Ref. [6]. The difference is a $\frac{2m}{\hbar^2}$ factor that we have added to get the oscillator strength of the transitions. It is such that summed over all transitions gives the total number of electrons in the system.

Several experimental techniques can be used to extract optical spectra of nanostructures, such as near-field optical microscopy, photoelectron spectroscopy, scanning tunnelling spectroscopy, or photoluminiscence. For the case of simple metal clusters a different method has been employed to measure the photoabsorption spectrum.[7,8] It is based on the fact that the clusters warm up and fragment upon absorption of light: the ratio between the number of clusters of a given size arriving at the detector with and without light is then proportional to the absorption cross section. In the case of metallic clusters, the process responsible for the fragmentation is the excitation of a collective mode, the so-called surface plasmon. All the valence electrons participate in this collective resonance, moving back and forth uniformly against the positive ionic background.[6,9] For sodium clusters, for example, the excitation energy of the surface plasmon is about 3 eV.

B. Sum rules

The full response is not required in some applications, and a knowledge of some moments m_k of the strength function $S(\omega)$ is sufficient to have a correct picture of the physical processes ($m_k = \int d\omega\omega^k S(\omega)$). For instance, the average frequency and the variance of the absorption spectrum can be obtained, respectively, as $\bar{\omega} = m_1/m_0$ and $\sigma^2 = (m_2/m_0 - m_1^2/m_0^2)$. A direct evaluation of the moments m_k is difficult, because the whole excitation spectrum is needed, but the even moments can be easily obtained within the random phase approximation (RPA).[6,10] By defining mean frequencies as $\omega_k = (m_k/m_{k-2})^{1/2}$, the bounds $\omega_1 < \bar{\omega} < \omega_3$ and $\sigma^2 \leq (\omega_3^2 - \omega_1^2)/4$ can be proved. Also $m_{-1} = \alpha/2$, where α is the static polarizability.[9] Consequently, one may estimate the centroid and the variance of $S(\omega)$ by evaluating the three

RPA moments m_{-1}, m_1 and m_3. The physical significance of the upper limit ω_3 is that of a rapid (diabatic) oscillation of the valence electrons against the ions, whereas the lower limit ω_1 is connected with a slow adiabatic motion of the electrons adjusting their density at any moment to the external field. This lower limit turns out to be a good estimate of the measured energy of the collective excitation for metallic clusters.[6,11] The moment m_1 represents the restoring force parameter for the collective translational oscillations of the electrons against the ionic background.[6] For a spherically symmetric electron density $n(r)$, m_3 is given by an overlap integral of the electronic and ionic densities. This integral is easily evaluated for a metallic cluster of radius R in the spherical jellium model[12] and for the particular case of an external dipolar excitation becomes $m_3 = \frac{e^4 Z}{\hbar m r_s^3}(1 - \frac{\delta Z}{Z})$ where $r_s = (3/(4\pi n_+^0))^{1/3}$, and δZ measures the spill-out of the electronic charge beyond the radius of the positive background. By neglecting the spill-out charge, then $\frac{\hbar^2}{m} m_{-1} = R^3$ (the classical dipolar polarizability of a metallic sphere is $\alpha = R^3$), and $\omega_3 = \sqrt{(\hbar^2 e^2 Z)/(m\alpha)} = \omega_0$ gives the resonance frequency of the classical Mie surface plasmon $\omega_{\rm Mie}$.[13]

The general expressions for the even moments corresponding to q- and l-dependent external fields $j_l(qr)Y_{l0}(r)$ are given in Ref. [14]. This field represents the angular decomposition of an incident photon, described as a plane wave $e^{i(\mathbf{qr}-\omega t)}$. With those operators one can analyze the multipolar response and also the inelastic scattering of electrons, relevant for electron energy loss spectroscopy (EELS). In small metallic clusters, and for fields of high multipolarity, there is a competition between the coulombic contribution to the response (diffusivity and collective excitations) and the kinetic energy contribution (single-particle excitations). The latter dominates for large angular momentum l or large momentum transfer q, indicating the vanishing of collective effects. The response of a metallic sphere to a photon of intermediate energy is dominated by dipolar excitations, and at large energies by electron-hole excitations.[6,14] As the size of the cluster increases, higher multipolar excitations start to dominate together with retardation effects (completely neglected until now).

II. TIME DEPENDENT DENSITY FUNCTIONAL THEORY (TDDFT)

To simplify our presentation we use in the following atomic units ($e^2 = \hbar = m = 1$).

The original formulation of the Hohenberg-Kohn-Sham density functional theory (DFT)[15,16] is not, in general, applicable to excited states or to problems involving time-dependent external fields, thus excluding the calculation of optical response properties, electronic spectra, quasiparticles, photochemistry, etc. However, theorems have now been proved for time-dependent density functional theory (TDDFT) which extend the applicability of the original theory. The first applications of TDDFT were actually done before its formal development and relied on analogies to time-dependent Hartree-Fock theory.[17] In this section we briefly present the foundations of TDDFT and refer the reader to the reviews in Refs. [1–4] for a deeper discussion of TDDFT and its applications. The main result of TDDFT is a set of time-dependent Kohn-Sham (TDKS) equations whose structure is similar to the time-dependent Hartree equations. However, the TDKS equations include all the many-body effects through a time-dependent exchange-correlation potential. This potential is unknow, and has to be approximated in any practical application of the theory.

The theoretical basis of TDDFT was laid by Runge and Gross,[18] and relies on the following theorem: *There exists a one-to-one mapping between time-dependent external potentials and time-dependent densities*. As a consequence of this theorem the expectation value of any quantum mechanical operator is a unique functional of the time-dependent density. From quantum mechanics we know that the time-dependent Schrödinger equation with the initial condition $\Psi(t_0) = \Psi_0$ corresponds to a stationary point (not necessarily minimum) of the quantum mechanical action integral

$$A[n] = \int_{t_0}^{t_1} \mathrm{d}t \langle \Psi(t) | \mathrm{i}\frac{\partial}{\partial t} - \hat{H}(t) | \Psi(t) \rangle \,. \tag{2.1}$$

(See Ref. [19] for an alternate definition that solves some problems related to causality.) From the previous one-to-one mapping between time-dependent potentials and densities, the action is a functional of the density $A[n]$ that must have a stationary point at the correct time-dependent density. Thus the density can be obtained by solving the Euler equation $\delta A[n]/\delta n(\mathbf{r},t) = 0$ with the appropriate boundary conditions. As in the static case, a time-dependent Kohn-Sham scheme can be introduced by considering a non-interacting system that reproduces the exact interacting density $n(\mathbf{r},t)$. The time-dependent Kohn-Sham equations read

$$\left[-\frac{1}{2}\nabla^2 + v_{\rm eff}(\mathbf{r},t)\right] \varphi_i(\mathbf{r},t) = \mathrm{i}\frac{\partial}{\partial t}\varphi_i(\mathbf{r},t) \,, \tag{2.2}$$

where $v_{\rm eff}(\mathbf{r},t) = v_{\rm H}(\mathbf{r},t) + v_{\rm xc}(\mathbf{r},t) + v_{\rm ext}(\mathbf{r},t)$ is the effective time dependent potential felt by the electrons. It consists of the sum of the external time-dependent applied field, the time-dependent Hartree term, and the exchange-correlation potential. The time-dependent density can be easily evaluated from the Kohn-Sham eigenfunctions

$$n(\mathbf{r},t) = \sum_{i=1}^{N} |\varphi_i(\mathbf{r},t)|^2 , \tag{2.3}$$

The advantage of the time-dependent KS-scheme lies in its computational simplicity compared to other quantum-chemical schemes such as the time-dependent Hartree-Fock or the configuration interaction (CI) methods.

A. Excitation energies in TDDFT

TDDFT has become the most popular method for the calculation of excitations in finite systems, both in physics (atomic, molecular and condensed matter)[1,4] and quantum

chemistry. As a first approximation to the excitation energies, one can simply take differences $\varepsilon_f - \varepsilon_i$ between the ground-state Kohn-Sham eigenvalues. Although this procedure is not entirely justifiable, it is often employed to obtain a first approximation to the excitation spectrum. It is well known that the Kohn-Sham eigenvalues and wave functions do not have a precise physical interpretation, with the exception of the eigenvalue of the highest occupied state, $\varepsilon_{\mathrm{HOMO}}$, that is equal to minus the ionization potential *IP* of the system.[20,21] In addition, Chong et al.[22] have shown that the orbital energies of other occupied levels of atoms and molecules can be interpreted as approximate, but rather accurate, relaxed vertical removal energies. It should be stressed that those relations are valid in exact DFT, but may fail for the approximate exchange-correlation energy functionals currently in use (e.g., the local density approximation underestimates $\varepsilon_{\mathrm{HOMO}}$ by roughly a factor of two).

Another approach, called Δ_{SCF} (delta self-consistent field), is based on the observation that the Hohenberg-Kohn theorem and the Kohn-Sham scheme can be formulated for the lowest state of each symmetry class.[23] An unrestricted variation will clearly yield the ground-state, but by restricting the variation to different symmetry classes it is possible to reach some excited states. The excitation energies can then be calculated from the difference in total-energy. However, this approach suffers from two drawbacks: i) only the lowest lying excitation for each symmetry class is obtainable, and ii) the exchange-correlation (xc) functional that now enters the Kohn-Sham equations depends on the particular symmetry we have selected. The excitation energies calculated in this way are only of moderate quality.

TDDFT allows to calculate the excited state energies of a many-body system based on information from an ordinary self-consistent DFT calculation. In the time-dependent approach, one studies the behavior of the system subject to a time-dependent external perturbation. The response of the system is directly related to the excited states of the *N*-particle system. The linear response of the system can be determined from the density-density response function χ, that is defined by

$$\delta n(\mathbf{r},\omega) = \int \mathrm{d}^3 r' \, \chi(\mathbf{r},\mathbf{r}';\omega)\delta v_{\mathrm{ext}}(\mathbf{r}',\omega) \qquad (2.4)$$

where δn is the density induced by the perturbing potential δv_{ext}. The same induced density can be calculated in the Kohn-Sham system

$$\delta n(\mathbf{r},\omega) = \int \mathrm{d}^3 r' \, \chi_0(\mathbf{r},\mathbf{r}';\omega)\delta v_{\mathrm{eff}}(\mathbf{r}',\omega)\,, \qquad (2.5)$$

where δv_{eff} includes the external field plus the induced Hartree and exchange-correlation potentials ($\delta v_{\mathrm{eff}}(\mathbf{r},\omega) = \delta v_{\mathrm{ext}}(\mathbf{r},\omega) + \int d^3 r' \frac{\delta n(\mathbf{r}')}{|\mathbf{r}-\mathbf{r}'|} + \int d^3 r' \frac{\delta V_{xc}(\mathbf{r})}{\delta n(\mathbf{r}')}\delta n(\mathbf{r}')$). The Kohn-Sham response function χ_0 describes the response of non-interacting electrons, and can be written in terms of the *gound-state* Kohn-Sham eigenvalues ε_i and eigenfunctions φ_i

$$\chi_0(\mathbf{r},\mathbf{r}';\omega) = \sum_{ij}(f_i - f_j)\frac{\varphi_i(\mathbf{r})\varphi_j^*(\mathbf{r})\varphi_j(\mathbf{r}')\varphi_i^*(\mathbf{r}')}{\omega - \omega_{ij} + i\eta} \qquad (2.6)$$

where $\omega_{ij} = (\varepsilon_j - \varepsilon_i)$ and f_i are Fermi occupation numbers. From Eqs. (2.4, 2.5) it is simple to derive a Dyson-like equation for the interacting response function. For a spin-unpolarised system it reads[24]

$$\chi(\mathbf{r},\mathbf{r}';\omega) = \chi_0(\mathbf{r},\mathbf{r}';\omega) + \int \mathrm{d}^3 r_1 \int \mathrm{d}^3 r_2 \, \chi_0(\mathbf{r},\mathbf{r}_1;\omega) \times \left[\frac{1}{|\mathbf{r}_1 - \mathbf{r}_2|} + f_{\mathrm{xc}}(\mathbf{r}_1,\mathbf{r}_2,\omega)\right]\chi(\mathbf{r}_2,\mathbf{r}';\omega)\,, \quad (2.7)$$

where we have introduced the so-called time-dependent exchange-correlation kernel

$$f_{\mathrm{xc}}(\mathbf{r},\mathbf{r}',\omega) = \left.\frac{\delta v_{\mathrm{xc}}[n(\mathbf{r},\omega)]}{\delta n(\mathbf{r}',\omega)}\right|_{\delta v_{\mathrm{ext}}=0}. \qquad (2.8)$$

Equation 2.7 has to be solved iteratively. Note that this scheme provides an exact representation of the full interacting linear density response.

Looking at the analytical structure of the interacting linear response function for a finite system it is easy to show that χ has poles at $\omega = \Omega$, where Ω are the excitation energies of the system.[25] As the external potential does not have any special pole structure as a function of ω, Eq. 2.4 implies that also $\delta n(\mathbf{r},\omega)$ has poles at the true excitation energies Ω. On the other hand, χ_0 has poles at the Kohn-Sham eigenvalue differences $\varepsilon_i - \varepsilon_j$. Exploiting these facts, one can derive an eigenvalue equation for the exact eigenmodes and eigenfrequencies of the system:[24]

$$\int \mathrm{d}^3 r' \, \Xi(\mathbf{r},\mathbf{r}',\omega)\xi(\mathbf{r}',\omega) = \lambda(\omega)\xi(\mathbf{r},\omega)\,, \qquad (2.9)$$

where the function Ξ is defined by

$$\Xi(\mathbf{r},\mathbf{r}',\omega) = \delta(\mathbf{r}-\mathbf{r}') - \int \mathrm{d}^3 x \chi_0(\mathbf{r},\mathbf{x},\omega)\left[\frac{1}{|\mathbf{x}-\mathbf{r}'|} + f_{\mathrm{xc}}(\mathbf{x},\mathbf{r}',\omega)\right]. \qquad (2.10)$$

This is a rigorous statement, that allows the determination of the excitation energies of the system from the knowledge of χ_0 and f_{xc}.

We now present a brief summary of the main approaches used to solve Eqs. 2.7 and 2.9 for the electromagnetic linear response calculation of nanostructured and low dimensional systems. For details we refer the reader to Refs. [2,24,26–28] for the matrix eigenvalue scheme, and Refs. [1,4,17] for the selfconsistent Green function approach. In the next subsection we will present in more detail another scheme based on the full solution of the time-dependent Kohn-Sham equations that can also be used to compute the linear response. This latter scheme is the main approach used in this work (unless otherwise stated).

1. Matrix eigenvalue method

The exact solution of Eq. 2.9 fully incorporates the collective electronic excitations. To solve the eigenvalue equation

one can expand $\xi(\mathbf{r},\omega)$ in an appropriate basis and solve numerically the resulting matrix-eigenvalue equation. For spin unpolarised systems using as basis the product of occupied and unoccupied orbitals[29] we find that the matrix equation to be solved is:

$$\left[\delta_{i,k}\delta_{j,l}\omega_{ij}^2 + 2\sqrt{f_{ij}\omega_{ij}}K_{ij,kl}^{(+,-)}\sqrt{f_{kl}\omega_{kl}}\right]\xi_{kl} = \Omega_{ij}^2\xi_{ij} \quad (2.11)$$

where $\omega_{ij} = \varepsilon_j - \varepsilon_i$, $f_{ij} = f_i - f_j$ is the difference of orbital occupation numbers, and the kernels for singlet (+) and triplet excitations (-) are given for example in Refs. [26,27]. An alternative way is to expand χ_0 around one particular energy difference between the Kohn-Sham eigenvalues of the occupied orbital k and the unoccupied orbital j. Assuming that the true excitation energy is not far away from $\varepsilon_j - \varepsilon_k$, it is sufficient to consider only the lowest order terms in those expansions. This leads for the singlet excitations to

$$\begin{aligned}\Omega &\simeq \sqrt{\omega_{kj}(\omega_{kj} + 2K_{ij,kl})} \quad (2.12)\\ &\simeq \omega_{kj} + 2\Re\langle\varphi_i^*\varphi_j|\frac{1}{|\mathbf{r}-\mathbf{r}'|} + f_{\rm xc}(\mathbf{r},\mathbf{r}',\omega_{kj})|\varphi_k\varphi_l^*\rangle\,,\end{aligned}$$

where $\Re$ indicates the real part of the expression. This single-pole approximation can be viewed as an attempt to correct the Kohn-Sham excitation energies individually without including collective electronic effects. Note that apart from the truncation of the expansions, two main approximations are necessary to calculate the excitation energies: (i) the static Kohn-Sham orbitals have to be calculated with an approximate static exchange-correlation potential, and (ii) the frequency-dependent exchange-correlation kernel has to be approximated.

The generalization of this formalism to spin is straightforward,[1,2] although the final expressions are more complicated than in the paramagnetic case that we have developed here. In the spin polarized case, the non-interacting Kohn-Sham response function is diagonal in the spin variables and exhibits poles at the Kohn-Sham energy differences corresponding to single-particle excitations within the same spin space. The mixing of spin-channels comes into play by the exchange-correlation kernel when building the interacting response function. The magnetization response naturally involves spin-flip processes.

2. *Selfconsistent Green's Function Method*

There is another traditional method[17] to calculate the excitations in linear response by self-consistently solving Eq. 2.7: this requires the evaluation of the independent-particle susceptibility χ_0. The expression for χ_0 involves an explicit sum over the complete energy eigenvalue spectrum of the Kohn-Sham effective potential. That is, not only the occupied orbitals are required, but also the unoccupied bound states and the continuum orbitals as well. This problem can be circunvented by calculating the Kohn-Sham response function from the expression[17]

$$\chi_0(\mathbf{r},\mathbf{r}';\omega) = \sum_{i=1}^{\rm occ}\left[\varphi_i^*(\mathbf{r})\varphi_i(\mathbf{r}')G(\mathbf{r},\mathbf{r}';\varepsilon_i+\hbar\omega) + \varphi_i(\mathbf{r})\varphi_i^*(\mathbf{r}')G^*(\mathbf{r},\mathbf{r}';\varepsilon_i-\hbar\omega)\right], \quad (2.13)$$

where the sum is now restricted to occupied states. The Kohn-Sham retarded Green's function is the solution of the Schrödinger-type equation

$$\left[\omega + \frac{1}{2}\nabla^2 - v_{\rm eff}(\mathbf{r})\right]G(\mathbf{r},\mathbf{r}';\omega) = \delta(\mathbf{r}-\mathbf{r}')\,. \quad (2.14)$$

The integral equation for the first order induced density (Eq. 2.5) is then solved iteratively. If the result of the first iteration is inserted into the Eq. 1.2 we obtain the independent particle approximation to the dynamical polarizability $\alpha(\omega)$. The photoabsorption cross section is then calculated directly from Eq. 1.3.

B. Full solution of the TDDFT-Kohn-Sham equations

Another very efficient method to calculate the optical spectrum of finite systems is based on solving directly the time-dependent Kohn-Sham equations in response to an external electromagnetic field. This method, originally used for the study of nuclear reactions,[31] was later applied to clusters[32–36] and biomolecules[37,38] and it constitutes the main body of applications of the present work.

The starting point for the time-dependent simulations is the Kohn-Sham ground state of the electronic system in the nuclear equilibrium configuration. To obtain the linear optical absorption spectrum one excites all frequencies of the system by applying the electric field $\delta v_{\rm ext}(\mathbf{r},t) = -\kappa z\delta(t)$. This is equivalent to giving a small momentum κ to the electrons.[31,32,34] The Kohn-Sham wave-functions at time δt are simply

$$\varphi_i(\mathbf{r},\delta t) = {\rm e}^{{\rm i}\kappa z}\varphi_i(\mathbf{r},0)\,. \quad (2.15)$$

These orbitals are then propagated in time

$$\varphi_i(\mathbf{r},t+\Delta t) = \hat{\rm T}{\rm e}^{-{\rm i}\int_t^{t+\Delta t}{\rm d}t\,\hat{H}_{\rm KS}(t)}\varphi_i(\mathbf{r},t)\,. \quad (2.16)$$

Note the presence of the time-ordered exponential due to the time-dependence of the Kohn-Sham Hamiltonian. In this method, only occupied states need to be propagated so there is no need of computing empty states. The spectrum can then be obtained using Eqns (1.2) and (1.3) from the induced dipole moments, and from the pertubation $\delta v_{\rm ext}$ The Thomas-Reiche-Kuhn sum rule can be used to check the quality of the calculations; another check is energy conservation, which the TDDFT respects when there is no external field applied. Similarly, the spin-spin response function can be computed to get the magnetic response of nanostructures (including non-collinear magnetism and magnon-like excitations).

It is also possible within a time-evolution scheme to calculate circular dichroism,[33] which is a very powerful tool used

in the characterisation of biomolecules. In particular the complex rotatory strength function $R(\omega) = R_x(\omega) + R_y(\omega) + R_z(\omega)$ is given in terms of the Fourier transform of the time evolution of the angular momentum operator $L_z(t) = \sum_i^{\rm occ} \langle \varphi_i | - {\rm i}(r \times \nabla)_z | \varphi_i \rangle$ (for magnetic circular dichroism one has to work with the total angular momentum instead of the angular part, but the equations remain the same). Results for the optical dichroism of DNA basis as well as other organic molecules are in rather good agreement with experiments.[38] It will be important, however, to address the role of different exchange correlation functionals for these chiro-optical properties.

One of the major advantages of this framework is that it can be trivially extended to handle non-linear response and nuclear dynamics. The set of equations to be solved for the combined electron and ion dynamics is formed by the time dependent KS Eqs. (2.2) together with Newton's equations for the motion of the ions

$$m_\alpha \frac{{\rm d}^2 \mathbf{R}_\alpha}{{\rm d}^2 t} = \mathbf{F}_\alpha(\mathbf{R}, t) \,. \tag{2.17}$$

The applied external field $v_{\rm ext}(\mathbf{r}, t)$ appearing in Eq. 2.2 is, in this case, the potential created by the nuclei plus a laser potential $v_{\rm laser}(\mathbf{r}, t)$ describing the classical time-dependent external electromagnetic field acting on the system. In the Newton equations for the ions, $\mathbf{R}_\alpha$ stands for the position of the ion labelled α, m_α for its mass, and $\mathbf{F}_\alpha$ is the instantaneous force on that ion. This force is calculated through the Ehrenfest theorem

$$\mathbf{F}_\alpha(\mathbf{R}, t) = - \langle \Psi(t) | \frac{\partial}{\partial \mathbf{R}_\alpha} \hat{H} | \Psi(t) \rangle \,. \tag{2.18}$$

This is just the extension of the Hellmann-Feynman theorem to the time-dependent domain. There are no Pulay corrections to this expression when the Kohn-Sham wave functions are expanded in a regular grid or in plane-waves; this would not be the case if one uses localized basis sets.[5,39]

C. Assessment of exchange-correlation kernels

As we have seen in the previous sections, one of the main ingredients in linear response theory is the exchange-correlation kernel. This is a complex quantity that includes all non-trivial many-body effects. Approximate kernels have been proposed over the past years and we consider here some of the most commonly used. The simplest and most used one is the ALDA (adiabatic local density approximation) kernel[40]

$$f_{\rm xc}^{\rm ALDA}(\mathbf{r}t, \mathbf{r}'t') = \delta(\mathbf{r} - \mathbf{r}') \delta(t - t') \left. f_{\rm xc}^{\rm HEG}(n) \right|_{n = n(\mathbf{r}, t)} \tag{2.19}$$

where $f_{\rm xc}^{\rm HEG}(n) = \frac{\rm d}{{\rm d}n} v_{\rm xc}^{\rm HEG}(n)$ is just the derivative of the exchange-correlation potential of a homogeneous electron gas (HEG) with density n. The ALDA kernel is local both in the space and time coordinates.[41]

Recently, Görling and coworkers have derived and implemented the exact-exchange kernel (EXX; see below) for solids.[42] Using the EXX, Kurth and Von Barth[43] have computed electronic excitations for atoms obtaining good agreement with experiment, and their results are encouraging for the development of new kernels having exact-exchange as an ingredient. A simplified version[44] of the EXX scheme has been applied to clusters and will be discussed below in the contest of the time evolution scheme.[34]

Another simplified kernel, in this case based on a simple analytical approximation to the EXX potential,[44,45] was derived by Petersilka, Gossmann and Gross (PGG) in Ref. [24]. The kernel has the form

$$f_{\rm x}^{\rm PGG}(\mathbf{r}t, \mathbf{r}'t') = -\delta(t - t') \frac{1}{2} \frac{1}{|\mathbf{r} - \mathbf{r}'|} \frac{\left| \sum_k \varphi_k(\mathbf{r}) \varphi_k^*(\mathbf{r}') \right|^2}{n(\mathbf{r}) n(\mathbf{r}')} \,. \tag{2.20}$$

As in the ALDA, this kernel is local in time.

Other kernels have been proposed in the literature, mainly to cope with deficiencies of the usual local approximations to describe the optical response properties of solids. One path was started in Ref. [46] in which the kernel was derived by imposing the TDDFT kernel to be static and equal, in the Bloch representation, to the screened coulomb interaction.[46,47] It is assumed that the Kohn-Sham wavefunctions coincide with the quasiparticle ones. Important excitonic effects for semiconductors are already obtained by using only the static long-range term $\Delta f_{xc}(q, G, G') = -\delta_{G,G'} \alpha / |q + G|^2$, where α is a numerical constant.[46] On similar grounds, the work of Ref. [48] has developed a robust and efficient frequency dependent and non-local f_{xc} imposing TDDFT to reproduce the many-body diagrammatic expansion of the Bethe-Salpeter polarization function. In contrast to previous work a closed-perturbative expansion of the kernel is provided that is of general applicability. The results for the optical and electron energy-loss spectra of wide-band gap insulators (LiF, SiO_2 and diamond) with strong excitonic effects are very well reproduced. Both spatial nonlocality and frequency dependence of the kernel are important in order to properly describe excitonic effects.

On the other hand, by using the approach of Sect. II B to calculate absorption spectra, the direct knowledge of the $f_{\rm xc}$ kernel is not needed as the excitation energies are obtained from the time-dependent density. In this case, the relevant quantity necessary to solve the Kohn-Sham equations, Eqs. 2.2, is the the time-dependent exchange-correlation potential. This potential is expected to be much simpler to model than $f_{\rm xc}$

The simplest approximation for $v_{\rm xc}(\mathbf{r}, t)$ is again the adiabatic LDA in which the static LDA exchange-correlation potential is used in the time-dependent Kohn-Sham equations, but evaluated with the time-dependent density. Following the same reasoning it is straightforward to construct adiabatic generalized-gradient approximation (GGA) potentials.[49] Unfortunately, the onset of absorption calculated either with the adiabatic LDA or most GGA functionals is typically below the observed ones (by several eV in the case of atoms). This problem is caused by the wrong asymptotic behavior of the LDA and GGA potentials: as the exchange term does not cancel exactly the self-interaction part of the Hartree potential, the potentials go exponentially to zero instead of having the correct $-1/r$ behavior for neutral systems. One GGA that does have the correct asymptotic behavior was derived by van Leeuven

and Baerends (LB94).[50] Although much better ionization potentials and energy eigenvalues are obtained in general with the LB94 potential, high-lying excitation energies are usually overestimated for small molecules, and the performance for low-lying states is less accurate than with the LDA.[51]

To overcome some of the shortcomings of explicit density functionals like the LDA and the GGAs, orbital-dependent xc-functionals can be used. For example the exact-exchange (EXX) functional is obtained by expanding the action functional of Eq. 2.1 in powers of e^2 (e is the electronic charge), and retaining only the lowest order term, that is, the exchange term, given by the Fock (action)-integral

$$A_{\rm x}^{\rm EXX} = -\frac{1}{2}\sum_{j,k}\int_{t_0}^{t_1} dt \int {\rm d}^3 r \int {\rm d}^3 r' \qquad (2.21)$$
$$\frac{\varphi_j^*(\mathbf{r}',t)\varphi_k(\mathbf{r}',t)\varphi_j(\mathbf{r},t)\varphi_k^*(\mathbf{r},t)}{|\mathbf{r}-\mathbf{r}'|}.$$

From this action functional one determines the Kohn-Sham potential by using the chain rule for functional derivatives.[45] This leads to an integral equation that determines the EXX potential. Unfortunately, this equation poses a hard numerical problem. There is, however, a approximation due to Krieger, Li and Iafrate (KLI),[44] that leads to a semi-analytical solution of the integral equation. Another example of an orbital-dependent functional is the self-interaction corrected local density approximation (SIC-LDA)[52]

$$A_{\rm xc}^{\rm SIC} = A_{\rm xc}^{\rm LDA}\left[n_\uparrow(\mathbf{r},t), n_\downarrow(\mathbf{r},t)\right] - \sum_\sigma\sum_i A_{\rm xc}^{\rm LDA}\left[|\varphi_i(\mathbf{r},t)|^2, 0\right]$$
$$-\frac{1}{2}\sum_\sigma\sum_i\int_{t_0}^{t_1} dt \int {\rm d}^3 r \int {\rm d}^3 r' \frac{|\varphi_{i\sigma}(\mathbf{r},t)|^2\,|\varphi_{i\sigma}(\mathbf{r}',t)|^2}{|\mathbf{r}-\mathbf{r}'|} \qquad (2.22)$$

In this functional, σ is the spin index. The first term is the LDA approximation whereas the second term subtracts the self-interaction part of the LDA exchange-correlation functional. The last term cancels exactly the self-interaction part of the Hartree term.

1. *Metal clusters*

The performance of the adiabatic functionals discussed above has been compared for small sodium and silane molecules.[34] All the calculated optical spectra of Na_2 (LDA, GGA, EXX, SIC-LDA and LB94) are quite similar, regardless of the exchange-correlation potential used. Those spectra show three peaks in the 2–5 eV range, and compare quite well with experiment, although the DFT peaks are all shifted towards higher energies by amounts ranging from 0.2 to 0.4 eV. The shift can be understood as resulting from the competition between the Coulomb repulsion contribution to the response and the electron-hole attraction in the exchange-correlation part. The functional giving the best results, although by a small margin, is the EXX, while the strongest departure from experiment is found for the LB94.

All the calculations for Na_4 shown in Fig. 1 yield similar spectra. The spectrum consists of three peaks in the 1.5–3.5 eV range, and a broader feature around 4.5 eV. The comparison with the experimental peak positions is quite good, although the calculated peaks appear, again, shifted to higher energies by 0.2 eV. The deviation of the LB94 is a little bit larger. In general the errors in the calculations with all these functionals are larger for the high energy peaks, which involve transitions to states near the ionization threshold. The figure also contains the results of a GW quasiparticle many-body calculation including excitonic effects.[53] These excitonic effects are large when screening is weak and, in fact, absorption occurs in Na_4 at energies substantially smaller than the quasiparticle gap.[54] In summary, Fig. 1 indicates good agreement with experiment for both the positions (within 0.2 eV) and the relative oscillator strengths of the main peaks of the photoabsorption spectrum.

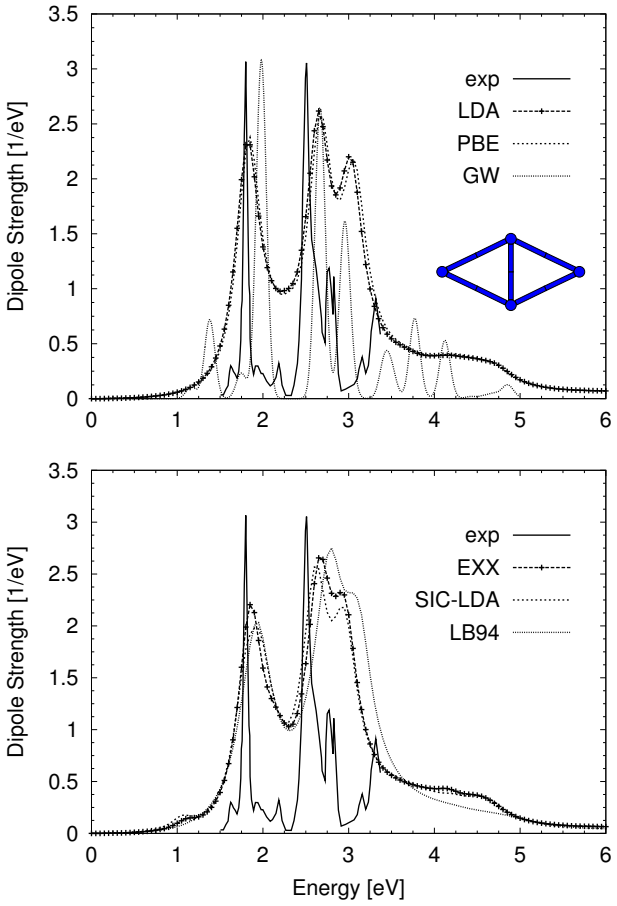

FIG. 1: Averaged dipole strength of Na_4. The curve labelled exp is the experimental photodepletion spectrum of Wang et al,[7] GW is the result of a many-body calculation including self-energy and excitonic effects,[53] and PBE indicates the results of GGA calculations with the functional of Ref. [49]. The other curves (LDA, EXX, SIC-LDA and LB94) correspond to calculations with functionals explained in the text. Adapted from Ref. [34] with permission of the American Institute of Physics.

2. Silanes

The two simplest hydrogen-terminated silicon clusters, silane (SiH_4) and disilane (Si_2H_6), pose a much harder challenge that the alkali clusters, due to the presence of *p* electrons and also due to the hydrogen atoms. As expected, the different exchange-correlation functionals lead to dissimilar results.[34] The HOMO-LUMO gaps obtained for SiH_4 with the different functionals are: 8.10 eV (LDA), 8.12 eV (GGA), 8.40 eV (LB94), 7.70 eV (SIC-LDA), and 8.77 eV (EXX). The differences between them are not large, although it is woth noticing that the smallest value is obtained for SIC, and the largest ones for LB94 and EXX . All those gaps are, however, smaller that the value of 13.0 eV obtained in a GW calculation.[55] For Si_2H_6 the HOMO-LUMO gaps are: 6.76 eV (LDA), 6.80 eV (GGA), 6.58 eV (LB94), 5.98 eV (SIC) and 7.17 eV (EXX), and again the variations are not large. Hovewer, the main difference between those methods is a nearly rigid shift of the spectrum of the LDA and GGA energy eigenvalues with respect to LB94 and EXX. The upwards shift leads to lower electronic binding energies. The SIC spectrum is also shifted, but much less.

The experimental absorption spectrum of silane,[56] shown in Fig. 2, has three peaks between 8 and 12 eV, followed by a much broader feature at higher energies. The spectra obtained with the LDA and GGA functionals (upper panel in Fig. 2) are quite similar to each other and the onset of absorption is underestimated by around 1 eV with respect to experiment. On the other hand, the SIC spectrum (given in the lower panel) is unphysically shifted to lower energies, and its first peak is split. The shifts of the SIC, LDA and GGA spectra could be anticipated from the low HOMO-LUMO gaps. The LB94 and EXX functionals behave quite well: the onset of absorption is now correct and the error in the position of the first three peaks is reduced by a factor of 2 from the LDA or GGA results. The LDA, GGA, LB94 and EXX spectra of disilane (Si_2H_6) are all very similar and consist of five peaks in the interval 7–12 eV, followed by a broader feature at higher energies. The overall comparison with experiment is slightly better than for silane. The SIC-LDA functional yielded again a quite unreasonable spectrum.

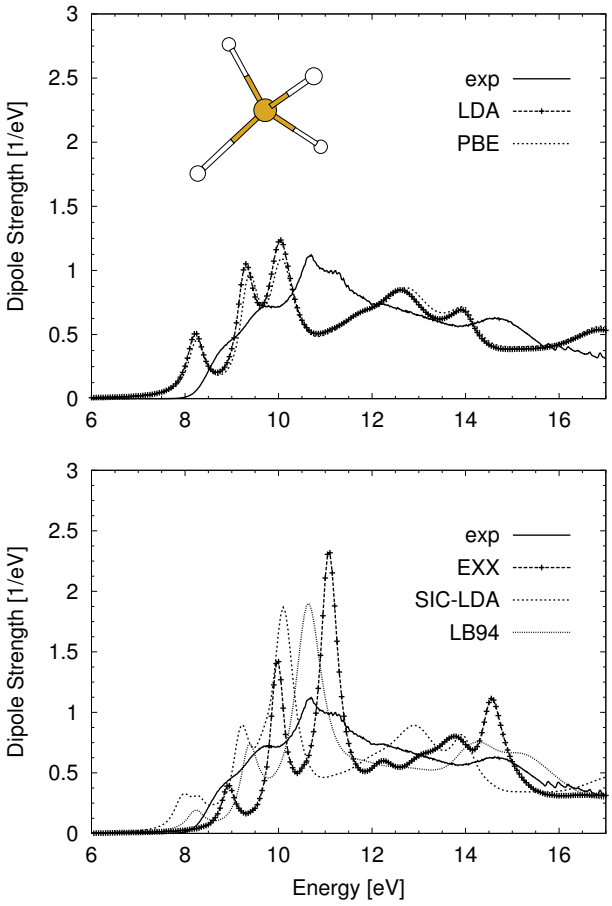

FIG. 2: Averaged dipole strength of SiH_4. The experimental curve (exp) is from Ref. [56]. PBE indicates the results of GGA calculations with the functional of Ref. [52]. The other curves (LDA, EXX, SIC-LDA and LB94) correspond to calculations with functionals explained in the text. Adapted from Ref. [34] with permission of the American Institute of Physics.

III. APPLICATIONS OF TDDFT

As the optical response of nanometer structures depends crucially on the particle size due to quantum effects, their absorption and emision spectra can be tuned by changing its size, opening the road towards potential applications in optical nanodevices. Therefore it is important to have a reliable scheme to address the calculation of response functions.

In the previous sections we dicussed optical properties of simple metal clusters and silanes to address the role of the exchange-correlation kernel. In this section we give a more comprehensive overview on different applications of TDDFT, in order to illustrate and reliability of this method, both for linear phenomena and for non-linear electron (ion) dynamics. In the case of nonlinear phenomena the present exchange-correlation functionals might not be accurate, but they nevertheless yield relevant information about the systems. Most of the results which follow have been obtained using the code `octopus`.[5] When other methods are used, this will be explicitly indicated.

A. Linear response processes

1. Optical response of atoms

The lowest singlet excitation energies of atoms of the alkaline earth and the zinc groups are given in Table I.[24,27] The LDA columns were obtained with the LDA exchange-correlation potential and the ALDA kernel. In the same way, the OEP columns correspond to the use of the OEP potential and the OEP kernel. First of all, the Table shows how the differences of energy eigenvalues, ω_{LDA} and ω_{OEP}, are corrected by using TDDFT (in the matrix eigenvalue implementation),

leading to improved excitation energies Ω_{LDA} and Ω_{OEP}. The Ω_{OEP} values are superior to the LDA results, and also better than the Δ_{SCF} values. The Δ_{SCF} excitations are obtained by subtracting the total energies corresponding to the ground state and excited configurations. Petersilka et al.[24] have argued that the main reason for the superiority of the OEP potential is that it is self-interaction free, and therefore has the correct asymptotic -1/r behaviour far from the nucleus, while the LDA exchange-correlation potential decays exponentially. From this argument, the importance of a good description of the static exchange-correlation potential becomes evident. A study of the excitation energies of the CO molecule[58] indicates again a good agreement with experiment.

TABLE I: The lowest singlet $^1S \rightarrow ^1P$ and triplet $^1S \rightarrow ^3P$ excitation energies of various atoms. The experimental values[57] are compared to TDDFT calculations in two approximations: the LDA and the OEP. The corresponding Kohn-Sham eigenvalues differences ω are given together with the results of a Δ_{SCF} calculation. For the case of triplet excitations we provide in parenthesis the results of the OEP plus LDA correlation. All energies are given in Rydbergs. Adapted from Ref. [24].

		Exp	$\Omega_{\rm LDA}$	$\Omega_{\rm OEP}$	$\Delta_{\rm SCF}$	$\omega_{\rm LDA}$	$\omega_{\rm OEP}$
Be	^{1}S→^{1}P	0.388	0.399	0.392	0.331	0.257	0.259
	^{1}S→^{3}P	0.200	0.192	0.138 (0.196)	0.181		
Mg	^{1}S→^{1}P	0.319	0.351	0.327	0.299	0.249	0.234
	^{1}S→^{3}P	0.199	0.209	0.151(0.196)	0.206		
Ca	^{1}S→^{1}P	0.216	0.263	0.234	0.211	0.176	0.157
	^{1}S→^{3}P	0.138	0.145	0.090(0.129)	0.144		
Zn	^{1}S→^{1}P	0.426	0.477	0.422	0.403	0.352	0.314
	^{1}S→^{3}P	0.296	0.314	0.250(0.280)	0.316		
Sr	^{1}S→^{1}P	0.198	0.241	0.210	0.193	0.163	0.141
	^{1}S→^{3}P	0.132	0.136	0.081(0.117)	0.135		
Cd	^{1}S→^{1}P	0.398	0.427	0.376	0.346	0.303	0.269
	^{1}S→^{3}P	0.279	0.269	0.211(0.239)	0.272		

However, Chelilowsky et al.[27] have pointed out that the differences between Ω_{LDA} and the experimental excitation energies are due to the approximations involved in Eq. 2.12. When the excitation energies are calculated by exactly solving Eq. (2.11) the experimental and theoretical results agree to within 5%–10% for all atoms. The encouraging conclusion is that the wrong asymptotic behaviour of the LDA potential appears not to be as important for the excited state properties as previously thought,[24,59] but more work needs to be done to clarify this point. In Table I we also report the calculated lowest triplet transition energies for the same atoms.[24] The TDLDA transition energies, calculated this time by solving exactly Eq. (2.11), are in better agreement with experiment than the results obtained by the OEP or $\Delta_{\rm SCF}$ methods. The OEP triplet transition energies are less accurate in this case, because the OEP potential does not include Coulomb correlation effects, which play a significant role for triplets. This is clear from the improvement of the triplet excitation energies once the LDA correlation functional is added to the OEP results (see the results between parenthesis in the column OEP of Table I).

a. Relativistic effects: As the atomic number of the atom increases, also does the error made by ignoring relativistic corrections. For atoms, the effect of relativity on the orbitals is well known: $s_{1/2}$ and $p_{1/2}$ orbitals are stabilized and contract, whereas d and f orbitals are destabilized and expand. It is also well known that this effect undergoes a local maximum at the coinage metals, known in the literature as the "gold maximum". The effect, for the gold atom, is illustrated in the inset of Fig. 4: the difference between the relativistic and non relativistic orbitals is depicted, both for the 6s and 5d orbitals. It may be seen how the s curve has a negative tail, which implies larger values for the non-relativistic orbital for large values of r: relativistic effects contract the orbital. The opposite effect (positive tail, i.e. expansion) takes place for the d orbital.

The Kohn-Sham eigenvalues also undergo strong changes as we change the level of approximation – relativistic or non-relativistic. These eigenvalues are given in Fig. 3 – the numbers are obtained either with our code `octopus` or with a relativistic atomic code. We plotted the 6s and 5d eigenvalues, as well as the ionization potential of the gold atom. The degree to which relativistic effects are included vary from left to right: the leftmost panel (NOT RELATIVISTIC) disregards relativity, and shows the values obtained in the LDA, SLDA, GGA and SGGA approximations (SLDA and SGGA stand for spin-polarized LDA and GGA, respectively). The next panel (RELATIVISTIC CORE) are the results obtained by making use of a relativistic pseudopotential. The panel REL. CORE + SO adds to the previous results the spin-orbit (SO) coupling correction (in this case spin polarization is assumed). Finally, the rightmost panel shows fully relativistic all electron calculations, both in the LDA and GGA approximations. The main conclusions that we can draw from the figure are: (i) adding the SO correction term to the non-relativistic Kohn-Sham equation yields eigenvalues in good agreement with the fully relativistic eigenvalues obtained from the Dirac's equation, as long as the pseudopotential core is relativistic; and (ii) the $s-d$ splitting is reduced dramatically by making use of relativistic pseudopotentials – no meaningful results will be obtained otherwise. However, for some observables such as the ionization potential, it suffices to use a relativistic pseudopotential, with no need of adding the SO correction.

We wanted to ascertain to which extent the relativistic effects influence the excited states of gold compounds by looking at the optical spectra. Previous considerations about the eigenvalues lead us to think that there is no need to use Dirac's equation, although adding the SO term should be relevant to obtain correct excitation energies. The absorption spectrum of the gold atom obtained with the octopus code is depicted in Fig. 4. The four curves correspond to LDA and GGA results with and without the SO correction. The arrows mark the first two experimental spectral lines. The main conclusions that can be drawn from Fig. 4 are:

- The SO term does have a definite influence on the spectrum. This is very apparent in the splitting of the first peak into the ^{2}P$_{1/2}$ and ^{2}P$_{3/2}$ lines, separated by ap-

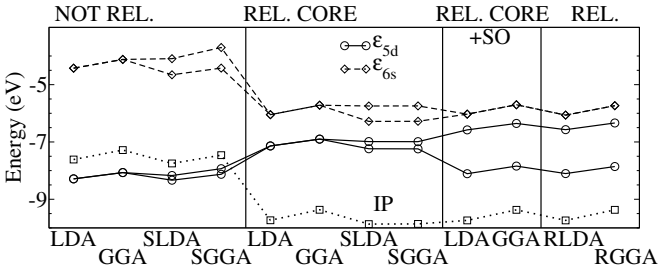

FIG. 3: 6*s* and 5*d* Kohn-Sham eigenvalues of the gold atom, in a variety of approximations (see text for details). Regarding the exchange and correlation approximation, the functional employed is indicated in the horizontal axis. SLDA and SGGA stand for spin polarized local density and generalized gradient approximations respectively. The dotted curve stands for the ionization potential, calculated by subtracting total energies, $\mathrm{IP} = \mathrm{E(Au)} - \mathrm{E(Au^+)}$.

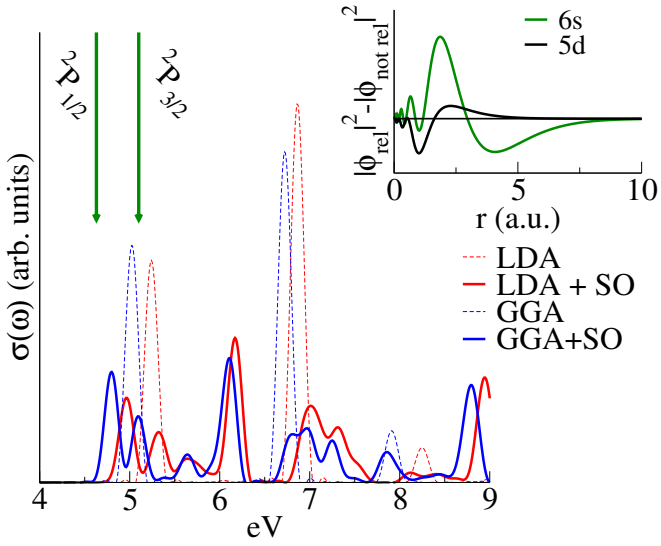

FIG. 4: Optical spectrum of the gold atom, calculated in the TDLDA and TDGGA approximations, with (thick curves) and without (thin, dashed curves) the spin-orbit coupling correction term. The arrows are the experimental spectral lines for the $^2P_{1/2}$ and $^2P_{3/2}$ excitations. Inset: Difference between relativistic and non-relativistic 6*s* (light) and 5*d* (dark) Kohn-Sham orbitals. The positive tail of the 5*d* curve shows its relativistic expansion, whereas the negative tail of the 6*s* curve shows the opposite effect. From Ref. [60].

proximately 0.5 eV. This splitting is underestimated by approximately 0.2 eV.

- There is a significant difference of 0.2–0.3 eV between LDA and GGA peaks. This is larger than the difference we obtain for lighter atoms. Hence we conclude that GGA should be employed in these systems.

- For higher energies (> 6 eV) the results deviate more from the experimental results. However, this may not be related to relativistic effects, but to the well known failure of both LDA and GGA functionals for energies lying above the HOMO of the system.

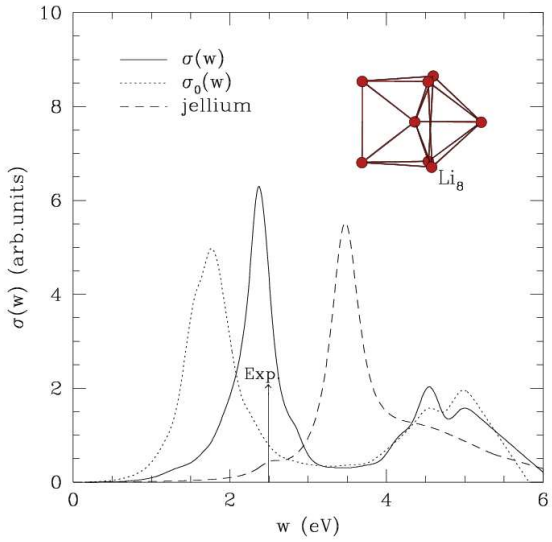

FIG. 5: Calculated TDLDA photoabsorption cross section of Li_8. The dashed line is obtained using the Jellium background model for the cluster. The dotted and the continuous lines correspond to calculations for the structure shown in the inset, using χ_0 and the fully-interacting χ response functions, respectively. The centroid of the experimental resonance from Ref. [63] is indicated by the arrow. Adapted from Ref. [61] with permission of the American Physical Society.

2. *Optical response of clusters*

a. Simple metal clusters The TDLDA photoabsorption cross section of Li_8 is given by the continuous curve in Fig. 5. The calculated ground-state structure, given in the inset, is a centered trigonal prism with an atom capping one of the lateral faces. The averaged value of the static dipole polarizability $(\alpha_{xx}+\alpha_{yy}+\alpha_{zz})/3$ is 97 Å^3, which is larger than the value of 63 Å^3 obtained in the spherical jellium model.[61,62] From classical arguments, a larger polarizability corresponds to a lower frequency of the collective dipole resonance, so a redshift of the resonance with respect to the jellium value of 3.5 eV should be expected. Indeed, the effect of explicitly accounting for the cluster structure produces a redshift of 1 eV which leads to very good agreement between the calculated resonance at 2.45 eV and the experimental value of 2.5 eV.[63] The nearly isotropic polarizability tensor explains the presence of a single collective-like resonance. The red shift can be tracked down to an increase of the electron effective mass, an effect of the Li ionic pseudopotential.

Other authors[27] have calculated the optical spectrum of small sodium clusters (Na_2, Na_4 and Na_8) using the matrix eigenvalue method. The results obtained from the exact calculation and two approximate expressions, the two single-pole approximations of Eq. (2.12), are reproduced in Fig. 6. The approximate expressions do not give a good account of the experimental data. On the other hand, the exact TDLDA calculation reproduces remarkably well the experimental spectral shape,[7,64] and the peak positions agree with experiment within

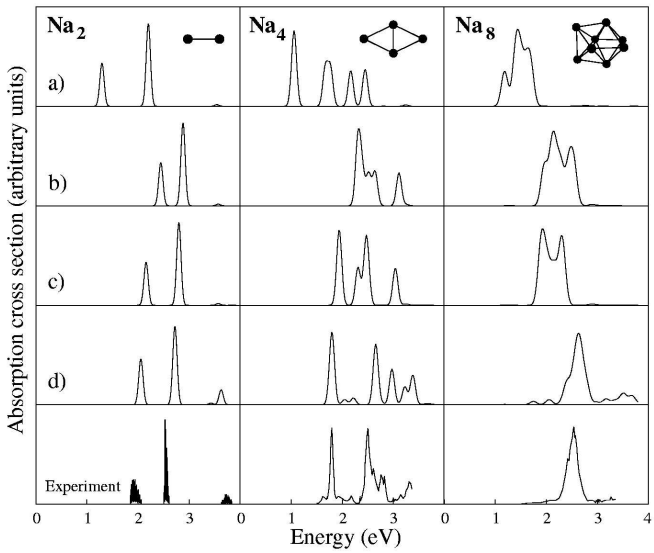

FIG. 6: Calculated and experimental absorption spectra of sodium clusters. (a) Absorption spectra from the difference of Kohn-Sham eigenvalues. The other plots show spectra calculated from the two single-pole approximation of Eq. (2.12) (b) and (c), respectively, and the full solution of the matrix Eq. (2.11) (panel d). All calculated spectra are broadened by 0.06 eV to simulate finite temperature. The experimental spectra are from Ref. [64]. Adapted from Ref. [27] with permission of the American Physical Society.

0.1–0.2 eV. The results are almost as accurate as the spectra calculated by the CI (configuration interaction) method.[65] For increasing cluster size the spacing between the discrete lines decreases, evolving towards the collective plasmon. For Na_8, with the rather spherical structure of a bicapped octahedron, a single peak is already obtained. The importance of electronic screening is evident by comparing the different panels in the Fig. 6.[66]

Very small mixed (Li_mNa_{4-m}) clusters have been studied by quantum chemical ab initio methods[68,69] motivated by the measurements of the optical absorption spectra of $LiNa_3$ and Li_2Na_2.[67] The photoabsorption spectrum is sensitive to m, that is, to the relative proportion of Li and Na atoms. The spectrum of Na_4 resembles that obtained from the Mie-Drude theory for an ellipsoidal droplet with three different axes. But, as Li atoms replace Na atoms, the deviations from the Mie theory increase. The measured spectra of $LiNa_3$ and Li_2Na_2 are explained by the ab initio calculations. The calculations also found low lying isomers for each Li_mNa_{4-m} case, corresponding to different ways of arranging the Li and Na atoms in the four vertices of the rhombus. The comparison between the experimental absorption spectrum of Li_2Na_2 and the spectra calculated for the three isomers of this cluster confirmed that the best agreement is obtained for the lowest energy isomer. On the other hand, the calculated spectra for the two singlet isomers of $LiNa_3$ are so similar that it was not possible to distinguish which isomer or whether a combination of both singlet isomers contributes to the measured spectrum. TDLDA calculations for the whole $Na_{8-m}Li_m$ family[70] obtained single (plasmon) peaks at both ends of the series, Li_8 and Na_8, consistent with a spherically symmetric electron density for both clusters. The replacement of one or two atoms in the homogeneous clusters produces an spheroidal deformation of the density and introduces extra shoulders in the spectrum.

b. Noble metal clusters: gold clusters To illustrate the role of spin-orbit in noble-metal clusters we have taken small gold clusters as an example. Relativistic effects are not only decisive for stabilizing the planar isomer as the ground state of these small clusters (as already reported by other theoretical studies[71]) but also for the proper description of the optical absorption spectra of the gold atom and gold clusters. In contrast to simple metal clusters, core polarization effects play here a fundamental role.[72] This is clearly manifested in the response of silver clusters, where the negative clusters exhibit the common redshift as the cluster size is decreased, whereas the positive clusters are blue-shifted.[73] A blue-shift of the plasma resonance as the size of the cluster is reduced has been found in the optical response of large (2-4 nm diameter gold nanoparticles supported in alumina.[74] The main effect of the d-electrons is to form a size-dependent polarizable background with dielectric function ε_d that strongly screens the valence electron interactions, giving rise to a reduction of the free-electron plasma frequency ($\sqrt{3/(2+\varepsilon_d)}\omega_{\rm Mie}$), where $\varepsilon_d \simeq 10$ for Au; this leads to a change in the main resonance peak from 5.2 eV in the simple jellium model to 2.5 eV in the improved model. From this discussion the general picture that emerges is that the optical response of large gold nanoparticles does not carry relevant information about the underlying ionic structure. However, as the cluster size reduces to less than 20 atoms, the specific ionic configuration starts to play a role and deviations from the simple picture of delocalized electrons moving in a polarizable background appear. This is clear from the catalitic activity of small supported clusters[75] and from the results presented in Fig. 7 and in Ref. [76]. It is important to remark that relativistic effects are much more important for both structural[71] and optical properties than the specific choice of exchange and correlation functional.

The details concerning our implementation of the spin-orbit effect in the octopus code will be provided in Refs. [60,76]. Here we add to the discussion of SO effects in the gold atom presented above, the case of the Au_4 cluster. The results of GGA calculations for two isomers of Au_4 are presented in Fig. 7, where the absorption spectra obtained with and without spin-orbit coupling in the hamiltonian are compared. In contrast to the case of the Au atom, the SO effect is minor in this cluster. In particular, there is a redistribution of oscillator strength in the low energy part of the spectrum, whereas the high-energy part is nearly unaffected by the SO coupling. Still this cluster is too small to show incipient plasmon-like excitations. Furthermore, the spectra carries relevant information on the structure of the cluster. The planar structure (top panel in Fig. 7) is dominated by two main sets of excitations at about 4 eV and 6.5 eV, whereas the more compact three-dimensional isomer has a broader spectrum with a clear transition at 3 eV absent in the planar isomer.

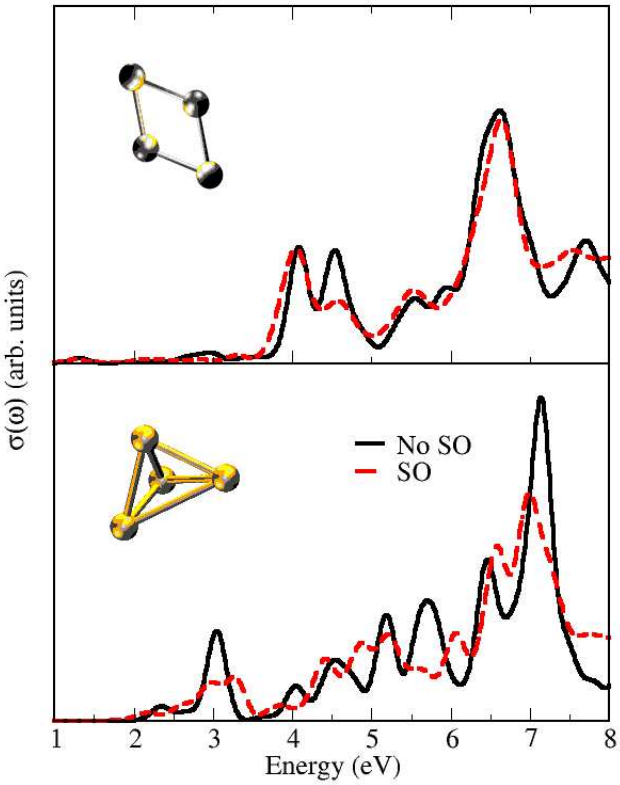

FIG. 7: Calculated GGA absorption spectra of Au_4 using the full solution of the time-dependent Kohn-Sham equations. Results are shown for two isomers for Au_4 with (dashed curves) and without (continuous curves) Spin-Orbit (SO) coupling in the hamiltonian. From Ref. [76].

c. Optical response of fissioning clusters Multiply charged metal clusters, like Na_N^{+q} are less stable than the corresponding neutrals due to the coulombic repulsion of the unbalanced positive charges, and can easily experience a process of fission. The process of cluster fission has close analogies to the fission of nuclei.[77] In both cases a charged droplet will become unstable towards the division into two or more fragments. In simple terms, the multiply charged cluster can be viewed as a droplet, which due to the unbalanced excess positive charge tends to deform through elongated shapes keeping the total volume constant. But the shape deformation increases the surface area and then the surface energy of the cluster. This builds up an energy barrier that prevents the spontaneous fission for large cluster sizes, even when the sum of the energies of the fission products is lower than the energy of the multiply charged parent. For small clusters, on the other hand, the coulombic repulsion may be so strong that there is no barrier, and fission occurs spontaneously. Optical spectroscopy has been proposed as a tool to follow the dynamics of fragmentation[78] as it provides a tool to analyze the various configurations along the fission path. It might be experimentally feasible to follow such a fission path by femtosecond time-resolved recording of the electronic response following short laser pulses, as done nowadays for mapping the isomerization paths of biological photoreceptors and chemical reaction paths of molecules.[79,80] One might even hope to have access to fission time scales and thus be able to estimate viscosity effects, in a way somewhat similar to the nuclear case.

3. *Thermal line broadening*

In order to compare with experiment, most TDDFT calculations perform an ad hoc broadening of the photoabsorption spectrum: the spectral lines, calculated for a static geometrical configuration of the cluster, are broadened through convolution with Gaussian or Lorentzian functions.[61,81] But a first principles description of absolute magnitudes, peak positions and line broadening can be achieved by calculating the photoabsorption cross sections along finite temperature molecular dynamics simulation trajectories. Shape fluctuations were introduced to account for the line broadening of simple metal clusters,[82] with good results for Na clusters. A step forward was taken in Ref. [83] by treating in perturbation theory the deviation of the ionic potential from being spherical. However, true first principles calculations have only been done recently by Moseler and coworkers,[84] who calculated the TDLDA optical spectra of Na_3^+, Na_5^+ and Na_9^+ at finite temperatures. The excitation energies were calculated by solving the eigenvalue Eq. (2.11) and averaging the calculated cross sections for a time propagation of 10 ps. The results are shown in Fig. 8. The structure of Na_3^+ is an equilateral triangle. Its calculated spectrum at T = 100 K, given by the histograms in panel (a) of Fig. 8, shows two peaks. The low energy peak originates from transitions ($\hbar\omega_1 = \hbar\omega_2 = 2.65$ eV) from the occupied *s*-like state to two empty *p*-like states with orbitals in the plane of the cluster. The three relevant orbitals are shown in the inset on the left of panel (a), where they are labeled as 1, 2 and 3 respectively. The other peak, centered at an energy of 3.41 eV, is due to the excitation to the other *p*-like orbital, perpendicular to the plane of the cluster (see the inset on the right side of the same panel). The positions of the two calculated peaks agree well with the experimental spectrum, given by the continuous line.[85] The intensity and width of the low energy peak are correctly predicted, but the measured high energy peak is less intense than the calculated one. The reason is that the experimental cross section is determined by measuring the photodepletion of the Na_3^+ intensity due to dissociation following the absorption of one photon. The two *p*-like states in the cluster plane are antibonding, so excitation into these states promotes dissociation, but excitation into the *p*-like state perpendicular to the cluster plane does not have a direct destabilizing effect. Thermal motion distorts the symmetry of Na_3^+ and lifts the degeneracy of the ω_1 and ω_2 transitions. The linewidth can be explained by the combined effect of (1) the line splitting caused by symmetry breaking, and (2) breathing vibrations (or spectral sweeping mechanism).

At a temperatute of 100 K the dynamics distorts the ground state D_{2d} symmetry of Na_5^+ and fragments the absorption line at 2.8 eV into two spectral lines (compare the oscillator strengths given in the upper-right inset in panel (b)). The

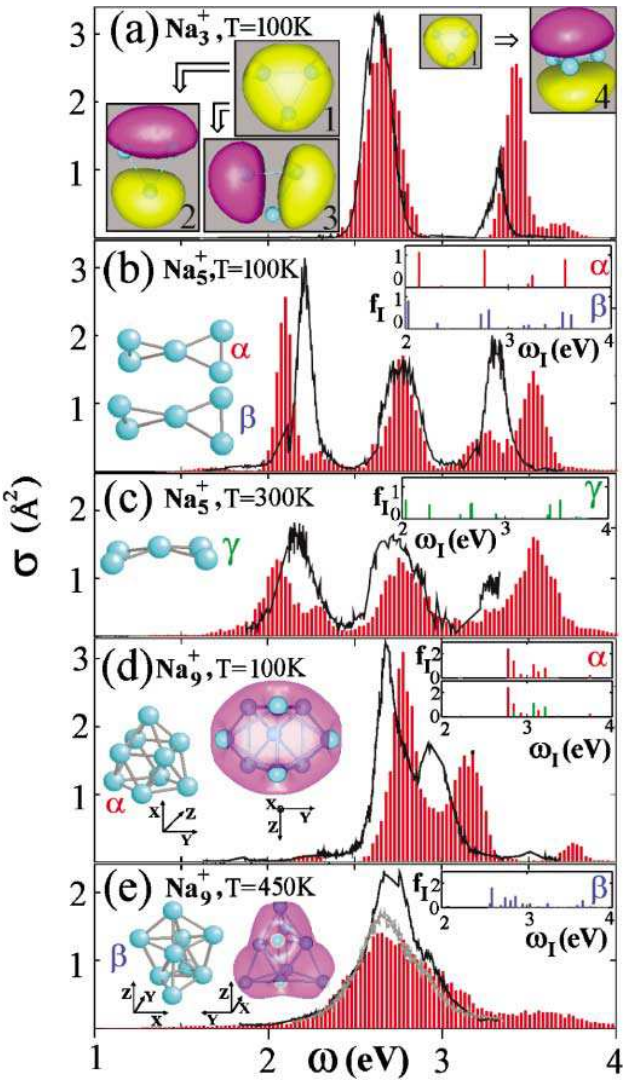

FIG. 8: Comparison of theoretical (histograms) and experimental (solid curves)[85] photoabsorption cross sections of Na_3^+ at 100 K (panel a), Na_5^+ at 100 K (panel b), Na_5^+ at 300 K (panel c), Na_9^+ at 100 K (panel d), and Na_9^+ at 450 K (panel e). Insets in panel (a) indicate constant density contour plots corresponding to electronic orbitals relevant for the discussion of the spectrum (see text). The contour plots in panels (d) and (e) correspond to the total electron density and reflect the shape of the cluster. Insets on the upper right sides of panels (b), (c), (d) and (e) give the oscillator strength for the cluster structures shown on the left side. Reproduced from Ref. [84] with permission of the American Physical Society.

increase of temperature to 300 K results in bent geometries (structure γ in panel (c)). In this case the low energy line at 2 eV is fragmented. All the lines are further broadened by the effect of the breathing modes. For larger clusters, thermal isomerization leads to another line-broadening mechanism, which adds to the other two discussed above. The ground state of Na_9^+ is oblate. Consequently the absorption lines are distributed in a bimodal manner, with further broadening arising from the line fragmentation and breathing mechanisms. By increasing the temperature to 450 K, the spectrum transforms to one with a single broad maximum. The main reason for the change in shape is the transformation between the ground state structure α (a tricapped trigonal prism) and the isomer labeled β. The static spectrum of this isomer is shifted to lower energies compared to that of the ground state, and the broad feature at 450 K is due to contributions from both isomers.

4. *Applications to carbon clusters*

The prototype of carbon clusters is the C_{60} fullerene. X-ray and energy-loss experiments[86] show the presence of two collective excitations, one around 28 eV (σ-plasmon) and the other around 6.3 eV (π-plasmon). These are seen in the photoabsorption cross section of Fig. 9, obtained from the direct solution of the TDDFT Kohn-Sham equations. The essence of these two experimental features can be understood in terms of the motion of electrons in σ-orbitals linking neighboring atoms in the C_{60} cage and π-orbitals extending in and out of the cage.[87] Two similar resonances have been observed for graphite (and are explained in the same way[88]) but not for diamond or amorphous carbon where only the higher one is observed. Photoabsorption data in the visible region[89] and photoionization cross sections (above 7.5 eV) have been reported for free C_{60},[90] and a collective excitation is seen at an energy of ∼ 20 eV with a linewidth of 10 eV. For an endohedral hydrogen impurity there is a shift of the π-plasmon to higher energy (∼ 8.1 eV) together with a substantial fragmentation on the low and high energy sides of the resonance. The main effect of an endohedral potassium impurity is to enlarge the linewidth of the resonance through a large fragmentation due to the proximity of particle-hole transitions.

Larger fullerenes are not longer spherical and exhibit interesting electronic and optical properties; for example C_{76}[33] is chiro-optical. In Fig. 9 we illustrate for the case of fullerenes the following fact known for metallic clusters: the form of the collective resonance of "delocalised-like" electron systems is dictated by the shape of the cluster. Therefore the spheroidal shape of C_{70} leads to a splitting of the low frequency π-like plasmon into two resonances, with the lower one for the external field applied along the long-axis direction of the cluster. The σ-plasmon is much less sensitive to the specific shape of the cluster, and its energy is very similar for both C_{60} and C_{70}. Furthermore, it does not depend on the direction of the applied filed with respect to the symmetry-axis of the cluster.

Medium size carbon clusters are predicted to have a wide variety of isomers with the form of cages, bowls, planar graphitic structures, rings and linear chains. The theoretical and experimental study of the different isomers may help to understand the way fullerenes form.[91] The smallest possible fullerene, C_{20}, consists of 12 pentagons with no graphitic hexagons intercalated. Other low energy isomers of C_{20} include a bowl, several rings and other closed 3-dimensional arrangements. The production of the cage and bowl members of the family has been reported in Ref. [92]. The smallest fullerene cannot be expected to form spontaneously, but has been produced from the precursor $C_{20}H_{20}$. The bowl was produced in the same way, and photoelectron spectroscopy has

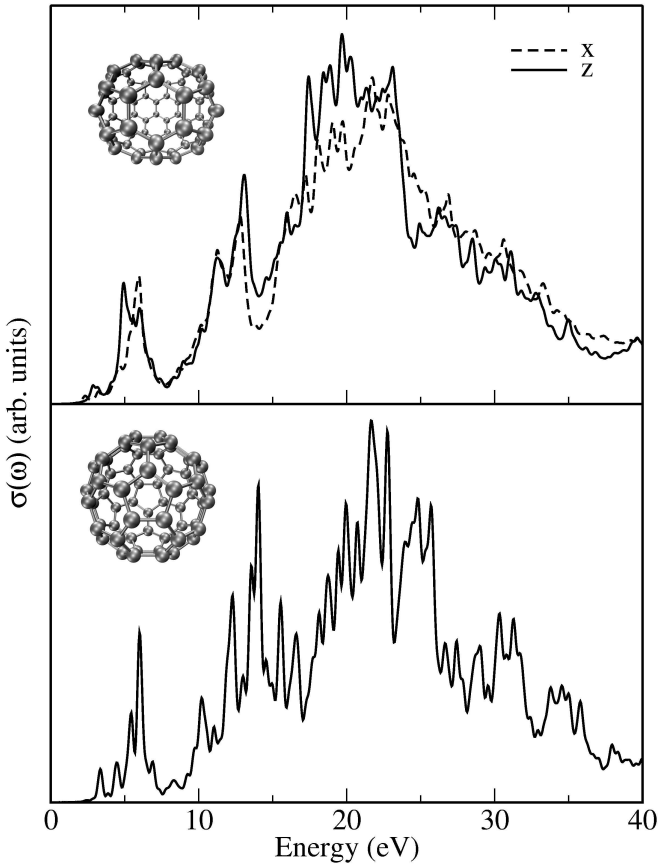

FIG. 9: Photoabsorption cross section, $\sigma(\omega)$ (in arbitrary units), for C_{60} (botton panel), and for C_{70} (upper panel) along the two principal symmetry axis. The long axis has been choosen along the z-direction. The cross sections have been obtained with the octopus code.

been used to distinguish between the different species. It is very difficult to make reliable theoretical predictions of the most stable structure of C_{20}. In fact, different levels of theory favor different isomers. At the Hartree-Fock level, the ring is the ground state, followed by the bowl and the cage.[93] Density functional theory in the LDA approximation reverses the order, predicting the cage as the lowest energy structure.[94,95] The use of better functionals based on the generalized gradient approximation (GGA) does not clarify matters: the ordering of the isomers depends on the particular correction used.[93–95] Quantum Monte Carlo (QMC) and coupled cluster (CC) methods have also been applied in an attempt to resolve the issue, yielding bowl-ring-cage ordering using the former method[93] and cage-bowl-ring using the latter.[96] Furthermore, it seems that the results are sensitive to the pseudopotential.[97] Another complication is that entropy effects affect the relative stability, and the calculated free energies as a function of the temperature[98] have been used to assign the dominant species produced by vaporizing graphite or prepared from precursors. Thus it is important to find experimental methods to determine the structure that are sensitive enough to be usable with the available cluster beam intensities, and optical spectroscopy fulfills the requirements. The geometrical structures of six members of the C_{20} family are given in Fig. 10: the smallest fullerene (cage), which is a Jahn-Teller distorted dodecahedron, the ring, the bowl, and three other cage-like structures, labeled as (d), (e) and (f). Structures (d) and (f), related by a Stone-Wales transformation,[99] are composed of four hexagons, four pentagons, and four four-membered rings. These structures are the six isomers with lower energy obtained by Jones within the LDA approximation.[100] Other structures, such as bicyclic rings, chains and tadpoles may be favored by entropy at high temperature and have been observed experimentally. However, neither of them seem to be a possible low temperature ground state.

TDDFT calculations of the optical absorption taken from Ref. [35] are shown in Fig. 10. While present experiments are not able to discriminate between the different spatial directions, the averaged spectra are still sufficiently different to discriminate between the different structures. Two regions can be distinguished in all the graphs: (a) the peaks which can be seen in the near ultraviolet, and (b) a broad absorption that starts at around 7.5 eV. Focussing attention on the lower energy peaks, the ring exhibits the largest optical gap and also the strongest collective transition. The bowl also has a high optical threshold, larger than 5 eV, but the intensity of the first significant transition is an order of magnitude weaker than in the ring. The relative intensities of the peaks, the fact that the first excitation is divided into two for the bowl, and the relative strength of the excitations in the 6–7 eV region, can all be used to distinguish the bowl isomer from the ring .

The spectra of the four three-dimensional isomers start at much lower energy and are more similar to each other, which is expected from their similar geometries. The fullerene isomer exhibits two peaks at 3.9 and 5.1 eV, with the second much stronger than the first one. Most of the strength concentrates above the ionization threshold (7.5 eV), and has a broad plateau starting at around 7 eV. This is different from the planar-like isomers, where an important fraction of the strength appears below 7 eV. Isomer (d) can be distinguished by the presence of a transition at quite low energy, 2.5 eV, as well as by the fragmentation into many states going up to 6 eV. Isomer (e) differs from the fullerene cage by the presence of a transition (labeled B in the Fig. 10) between the transitions that would be seen in the cage. The spectrum of isomer (f) is similar to that of the fullerene cage up to the second peak, but it is shifted down by about 0.3 eV. Isomer (f) also has a third peak near 6 eV, in a region where there is a gap in the spectrum of the fullerene cage, and that difference would be definitive.

5. *Benzene*

As an example of an organic molecule, the results for the benzene molecule C_6H_6 are shown in Fig. 11. The main features are: (i) a narrow peak at about 7 eV, that corresponds to the transition between the π and π^* orbitals (these orbitals are shown in the figure), a characteristic of Carbon conjugated compounds, and (ii) the broad feature above 9 eV, which corresponds to the $\sigma \rightarrow \sigma^+$ transitions. The TDDFT method

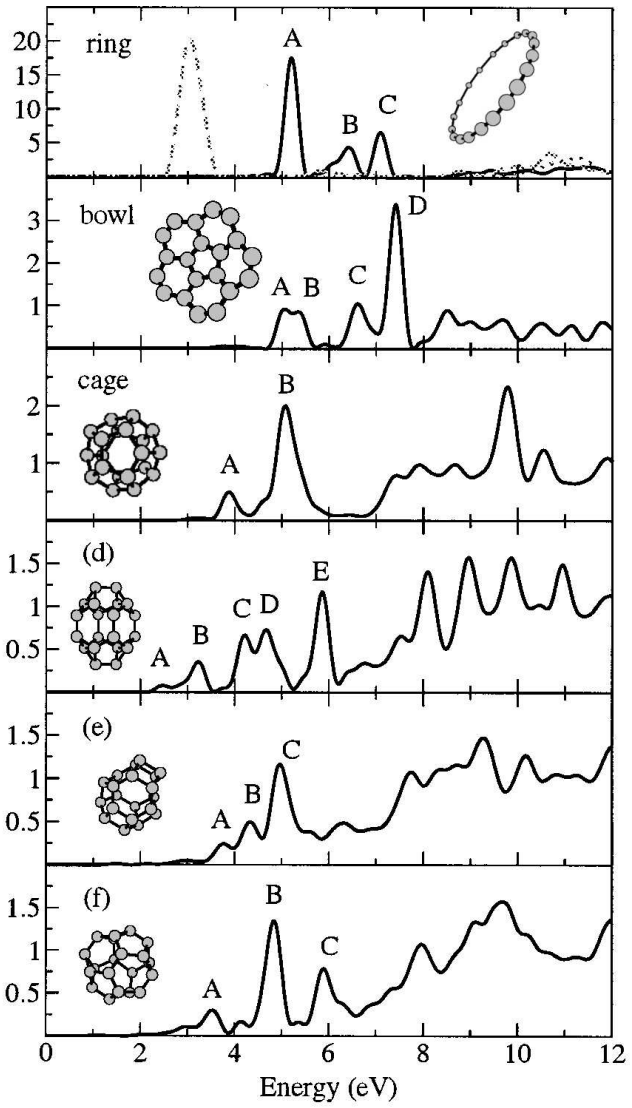

FIG. 10: Dipole strength function, in eV^{-1}, for several isomers of C_{20} obtained with the octopus code. The dipole strength functions have been averaged over all orientations of the system. The dashed line in the upper panel corresponds to the independent particle approximation. Adapted from Ref. [35] with permission of the American Institute of Physics.

seems to work well for all organic molecules, at the LDA level for the low lying excitations, and by making use of more corrected functionals for high energies.[101] The quality of the calculations for large π-conjugated systems remains open, as recent studies show some deficiencies of the usual exchange-correlations functionals for linear condensed acene molecules.[102]

6. *Applications to biomolecules*

Besides the spectacular advances over the last years in the characterisation of structural and dynamical properties of

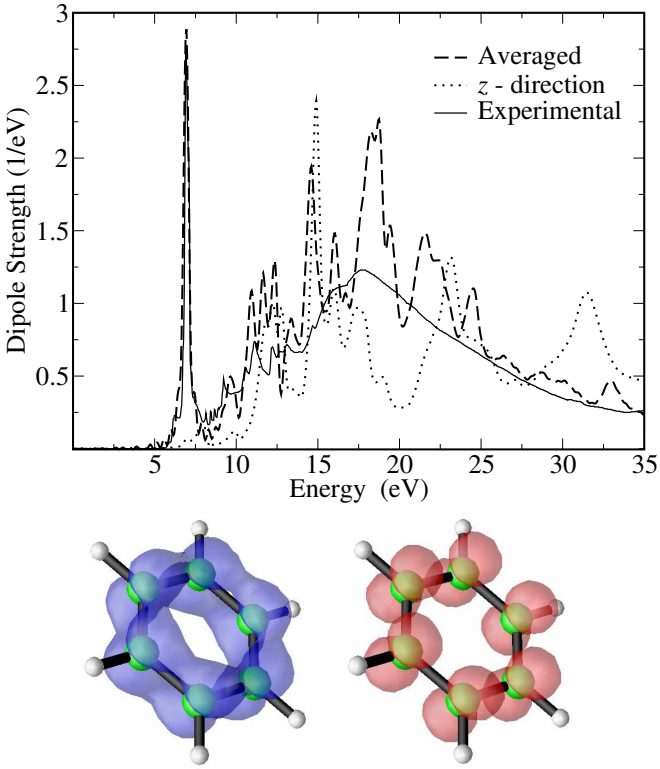

FIG. 11: Optical absorption of the benzene molecule obtained with the octopus code. The experimental result is from Koch.[103] The bottom panel shows the HOMO (π) and LUMO (π*) Kohn-Sham orbitals, respectively. Transitions between these two states are responsible for the large absorption peak at 7 eV. Reproduce from From Ref. [5] with permission from Elsevier.

biomolecules by a combination of quantum mechanical and classical molecular mechanics methods, the theoretical understanding of the interaction of those molecules with external time-dependent fields is in its infancy in spite of the large amount of experimental work on photoactive molecules. In particular, processes related to vision and photosynthesis rely on a subtle interplay between optical absorption in the photoactive center and its decaying mechanism through the coupling to the internal vibrational modes of the molecule, including isomerization processes as well as coupling to the environment (supporting protein and solvent).

In this context the green flourescent protein (GFP) has been studied experimentally in various environments (in solution as well as *in vacuo*), and has been found to exhibit a rich and complex behavior that is the subject of much current debate. The measured optical absorption spectrum of the wild type (wt) GFP shows two main resonances at 2.63 and 3.05 eV[104,105] (see Fig. 12), that are attributed to two different thermodynamically stable protonation states of the chromophore (neutral and negative configurations of the chromophore, respectively). So far, ab initio quantum chemistry has not been able to provide satisfactory agreement with the spectroscopic data, and thus has not contributed too much to confirm or rule out various possible scenarios of photodynamics in the GFP. A good description of the optical prop-

erties of the GFP photorreceptor has been achieved[37] using an approach combining (a) a quantum-mechanical molecular-mechanics (QM-MM) method to obtain the structure with (b) time-dependent density functional theory to treat the electronic excitations. The structures were optimized using a hybrid quantum mechanical-molecular mechanics (QM-MM) method[106–108] with a semiempirical hamiltonian[109] to describe the quantum subsystem. The QM region was formed by three amino-acid sequences, Ser65, Tyr66 and Gly67. The optimized structure of the chromophore with the most important neighbor residues is shown in Fig. 12. On the other hand, the anionic form of the chromophore was obtained by deprotonation of the Tyr66 and protonation of Glu222. The computed photoabsorption spectra of the GFP neutral and anionic chromophores, shown in Fig. 12, are in excellent agreement with experiment assuming the presence of the two forms of the photo-receptor, protonated and deprotonated respectively, in an approximatly 4:1 ratio. Furthermore, it can be seen in the inset of Fig. 12 that light polarized along the x-direction is responsible for the lowest optical transition in the neutral chromophore. The molecule is nearly transparent to visible light polarized along the other two orthogonal directions. The GFP turns out to be a rather anisotropic molecule in the visible region, a property that could be used to enhance the photo-dynamical processes in well oriented GFP samples for opto-electronic devices. The new approach developed holds great promise for future applications in biochemistry and biophysics as it is able to handle not only the optical response but also ultrashort femtosecond electron-ion dynamics. Preliminary calculations[38] for the optical spectra of the DNA basis are also in excellent agreement with available experimental data.

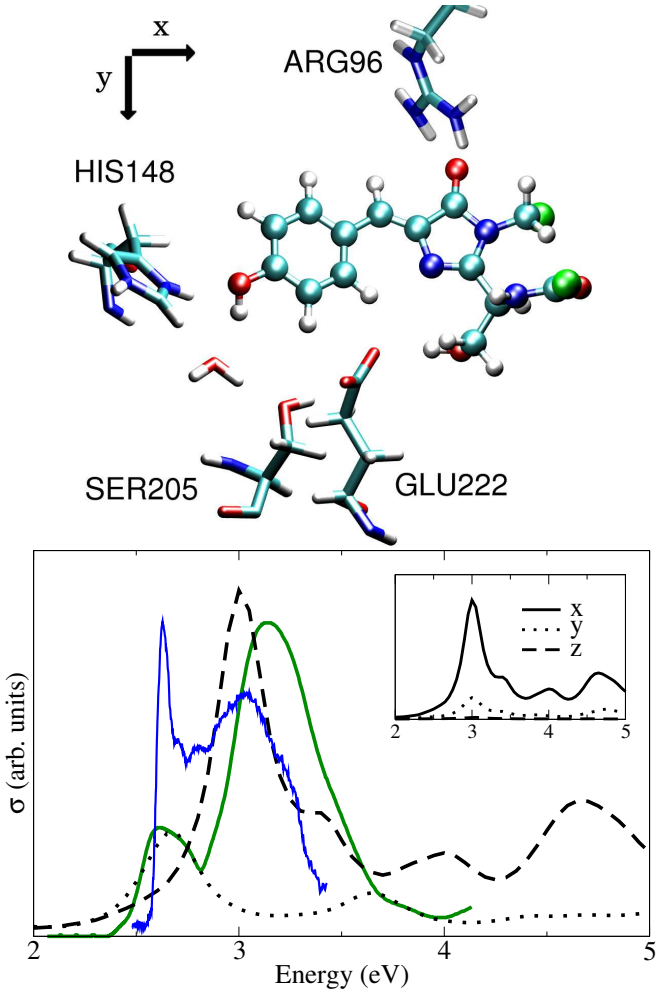

FIG. 12: Top: Optimized structure of the neutral chromophore and its closest charged residues inside the green fluorescent protein (GFP): His148, Arg96 (positive) and Glu222 (negative). Bottom panel: Computed photoabsorption cross section of the neutral (dashed line) and anionic (dotted line) chromophores. For comparative purposes the anionic results have been divided by 4. Experimental results at 1.6 K (dark thin solid lines)[104] and room temperature (light thick solid line)[105] are also given. The inset shows a decomposition of the calculated spectrum of the neutral chromophore in the three directions, showing the inherent anisotropy of the green fluorescent protein molecule. The theoretical spectra have been calculated with the octopus code. Adapted from Ref. [37] with permission of the American Physical Society.

B. Nonlinear processes

For the purposes of obtaining nonlinear optical properties, we follow the evolution of the system under the influence of a laser field (treated in the dipole approximation). The emitted harmonic spectrum can then be calculated from the acceleration of the dipole moment.[110,111] Furthermore, electron-ion dynamics ("non-adiabatic") is quite relevant in a first-principles description of the laser control of chemical reactions. This topic is currently attracting considerable experimental and theoretical attention.

1. *Electron ion-dynamics of a van der Waals complex: Ba..FCH$_3$*

In order to understand the physical mechanisms underlying the electron/ion dynamics of the Ba..FCH$_3$ complex, extensive excited state simulations were performed within a TDDFT formalism.[112]. The initial configuration for studying the laser induced reactivity is the ground state of the weakly bound Ba..FCH$_3$ complex. For the relaxed molecular structure, rather good agreement was noticed with previous CI calculations[113] (differences of about 2% in the bondlengths) and ionization potential (the calculated value is 4.9 eV and the measured one 4.66 eV). Before discussing the combined electron-ion dynamics, we show in Fig. 13 the calculated optical absorption cross section of Ba..FCH$_3$. A very good agreement with available experimental data (also shown in the Figure) is obtained. The visible spectrum is dominated by a single peak around 2 eV that is used afterwards to trigger and control the chemical fragmentation of this complex. It is interesting to note that the main peak of the spectrum corresponds to a HOMO-LUMO like transition with major weight on the Ba atom. However this $6s-6p$ atomic-like transition of the Ba atom has been redshifted with respect to the calcu-

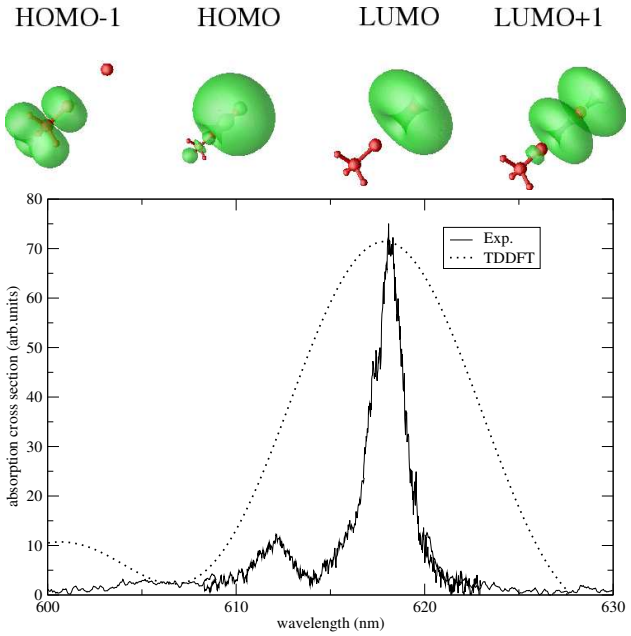

FIG. 13: Top: two lowest unoccupied (LUMO and LUMO+1) and two highest occupied (HOMO and HOMO-1) orbitals of the Ba..FCH_3 molecule. The HOMO-LUMO orbitals are mainly located on the Ba atom. Bottom: comparison between the computed and measured[112] optical absorption spectra. The strongest absorption peak can be assigned to the HOMO-LUMO transition. The agreement is very good taking into account the accuracy of the calculated spectrum (about 0.1 eV). Reproduced from Ref. [112] with permission of EDP Sciences.

lated isolated Ba absorption to 2.4 eV. This renormalization of the atomic transition stems from the polarization of the atomic cloud around the Ba atom due to the dipole of the FCH_3 part (this is clearly seen in the shape of the HOMO-LUMO orbitals in Fig. 13). The difference of HOMO-LUMO eigenvalues is 1.6 eV, therefore the Coulomb plus exchange and correlation effects induce a blueshift of this independent-particle transition of about 0.4 eV. From this discussion it is clear that the static electronic properties of this complex are well described by the present approach.

The theoretical simulation performed in Ref. [112] provides a clear picture of the cluster photodissociation mechanism, whose main features are the following: First, the pump laser excites the HOMO-LUMO transition of the molecule. This excitation is mainly localized on the Ba atom (see Fig. 13). Although this is the main excitation effect, in the short time scale the laser also populates other Born-Oppenheimer surfaces that play a role in the ensuing dynamics. Then, the coupling of this electronic excitation to the ions brings the molecule to an excited vibrational state. The time scale for this coupling process in the simulation is of the order of 100–300 fs. During this vibration the laser continues to act and, eventually, leads to the detachment of the BaF fragment from the remaining complex. If the probe laser is applied shortly after the pump laser, the excited state does not have time to decay into the excited-state molecular vibration, and then as product we get the ionized Ba..FCH_3^+ fragment. Only when the delay between pump and probe is above 100 fs we observe the appearance of the BaF^+ and Ba^+ fragments. It is important to emphasize that with only the pump laser and for all laser power densities, polarization and initial configurations, no signal of the non-reactive channel (Ba fragment) is observed in the simulations and only the BaF fragment is obtained. This is in agreement with the fact that no Ba^+ ion signal was observed with the pump laser only, even though high fluences were employed.

2. *Photofragmentation: the case of the noble gas molecule He_3^+*

The photofragmentation of a singly ionized helium trimer is also a challenging problem. We have performed simulations of this process for He_3^+,[36] motivated by the fact that this system has been studied previously. The geometry has been predicted to be a symmetric linear trimer[114] by ab initio methods. The optical spectrum has been characterized both experimentally[115] and theoretically.[116] Haberland et al.[117] have performed experiments studying the photodissociation of ionized rare gas trimers, including He_3^+, induced by a 10 ns laser pulse, with photon energies ranging from 1.5 to 6 eV. Their results support the picture of a linear trimer photo-excited to a totally repulsive state, coupled to the ground-state through a parallel transition moment: the two lateral atoms are expelled with high opposite velocities, whereas the central atom only gains a small velocity at either side. The positive charge generally localizes on one of the fast outer particles. The relevant potential energy curves are shown in Fig. 14. TDLDA calculations of the optical response have been performed varying the nuclear geometry along the dissociation coordinate. The inset of the Fig. 14 shows the optical absorption spectrum for the equilibrium geometry. It is clear that only one excited potential energy surface is of interest; the only relevant optical transition is the $\Sigma_g \rightarrow \Sigma_u$ at 5.0 eV. The experiments position this peak at $\approx$ 5.3 eV. This excited PES is totally repulsive, and photoinduced population of this state should lead to dissociation.

In Ref. [36] we have presented a number of simulations of the response to a laser pulse using various sets of laser parameters, and some results are shown in Fig. 15. The shape of the laser pulse was trapezoidal in all four cases: an ascending linear ramp from 0 to $\approx$ 2.5 fs, a plateau of 25 fs, and then a descending linear ramp again of $\approx$ 2.5 fs. Intensities and frequencies, on the contrary, are different. The top panels depict non-resonant conditions, at one third (left) and five thirds (right) of the resonance $\Sigma_g \rightarrow \Sigma_u$ (5 eV). In both cases the two outer atoms only oscillate slightly around the equilibrium positions. The bottonm panels represent resonant conditions with varying intensities. Two different dissociative channels are observed. In the left panel, a low laser intensity is provided, and the picture corresponds with the findings in Ref. [117] – the two outer atoms gain high opposite velocities, whereas the central one remains almost unperturbed (note that the intensity is the same as the one used in the upper panels, where no dissociation was obtained). A higher intensity was used for the simulation shown in the botton-right panel, and

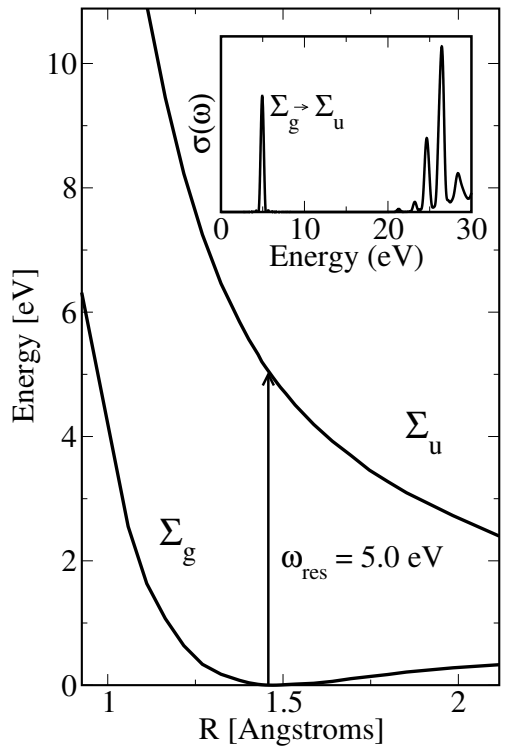

FIG. 14: Σ_g (ground state) and Σ_u potential energy surfaces. The abscissa corresponds to the simultaneous and symmetric displacement of the two outer atoms along the linear trimer axis. Inset: TDLDA calculation of the photoabsorption cross section at the equilibrium geometry. Reproduced from Ref. [35] with permission of EDP Sciences.

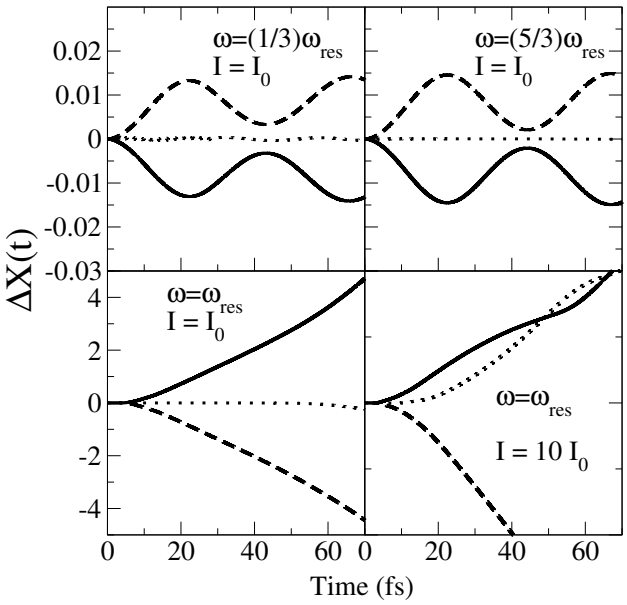

FIG. 15: Time-evolution of the three nuclear displacements (solid: top atom; dots: central atom; dashed: botton atom) with respect to their original positions, along the linear trimer axis, for the frequencies and intensities given ($\omega_{res} = 5$ eV, $I_0 = 8.8 \times 10^{11}$ Wcm^{-2}). Reproduced from Ref. [35] with permission of EDP Sciences.

in this case the trimer dissociates into a dimer and an isolated atom. Most likely, the intensity of the nanosecond laser pulse used in the experiment is low, which agrees with the symmetric dissociative picture of the botton-left panel. This prediction would need further experimental confirmation.

3. Clusters in strong laser fields

Progress in laser technology has opened new lines of research in the domain of non-linear cluster dynamics. Lasers offer an ideal tool for spanning various dynamical regimes, ranging from the linear regime with plasmon-dominated dynamics, to the semi-linear regime of multi-photon absorption processes[118,119] and the strongly non-linear regime of Coulomb explosion.[120,121] From the theoretical side, only theories based on DFT have been able to deal with such different situations and dynamical regimes for clusters.[122] In addition to the irradiation by intense femtosecond laser pulses,[123] one can consider another class of rapid, intense, excitations: collisions with energetic highly-charged ions.[124] In both cases the excitation takes place in times between tens of femtoseconds down to below 1 fs. This time is directly comparable to characteristic time scales of the valence electron cloud, and consequently the cluster response is primarily of electronic nature. The first phase of the reaction is a direct emission of electrons and an oscillation of the collective plasmon (time scales of the order 1–10 fs). In a second stage, still of purely electronic nature, damping of the collective electronic motion takes place, both by means of Landau-like damping and by electron-electron collisions. The time scales associated to these effects are variable depending on the cluster size (Landau-like damping) and the deposited excitation energy (electron-electron collisions). Landau-like damping takes 10–20 fs and collisional effects around 10–100 fs. After that, the electronic degrees of freedom slowly couple to the ionic motion, and may lead to the explosion of the charged cluster on longer times, of several hundred femtoseconds. Two mechanisms operate here: the first one is the coulombic repulsion due to the net charge of the cluster following ionization, and the second corresponds to energy exchanges between the hot electron cloud and the still cold ions. The two effects interfere constructively to activate ionic motion and to lead to evaporation, fission or fragmentation. Thermal evaporation of electrons proceeds on a very long time scale, usually slower than ionic processes like monomer evaporation and fragmentation. It can become competitive in the 100 fs range only for very hot clusters. Indeed, experiments in platinum clusters suggest that the highly-charged cluster rapidly undergoes a Coulomb expansion, with a time scale of 100–500 fs.[121] An interference can thus occur between the laser pulse and the ionic motion, which may enhanced the ionization.

We now illustrate the various stages of the excitation and response of metal clusters in the non-linear regime. The excitation of the cluster Na_{41}^+ subjected to a long laser pulse (240 fs) of frequency 2.86 eV, shows how the ionic motion can inter-

fere with the excitation process. The excitation of this cluster has been simulated using the TDLDA.[125] The results are presented in Fig. 16. The third panel, giving the number of electrons emitted, N_{esc}, shows that ionization takes place in several steps. In a first phase, lasting for about 80 fs, the response is fully electronic, and is characterized by low ionization. But the net charge of the cluster shifts the plasmon resonance upwards until it comes into resonance with the laser. This results in a sudden increase in ionization at around 100 fs, leaving the cluster in a state with a net charge +5. From then on, ionization proceeds at a slower pace until another burst of electrons shows up at 250 fs, stripping again about 5 electrons. The lowest panel of Fig. 16 gives the electric dipole signal $D(t)$. It is clear that large slopes in ionization (N_{esc}) are correlated with large dipole amplitudes, which again reflects resonant conditions. A relation between the two observables is observed by plotting in the second panel the instantaneous plasmon frequency calculated at each time t for the instantaneous structure and charge of the cluster. The correlation between large slopes in N_{esc} and resonant conditions is noticeable. The first coincidence at time 100 fs reflects the blueshift of the plasmon due to the first stage of ionization. The Coulomb expansion leads to a redshift of the resonance, which is responsible for the second coincidence at 230 fs. The system thus acquires a much higher charge state and ends up in a violent Coulomb explosion.

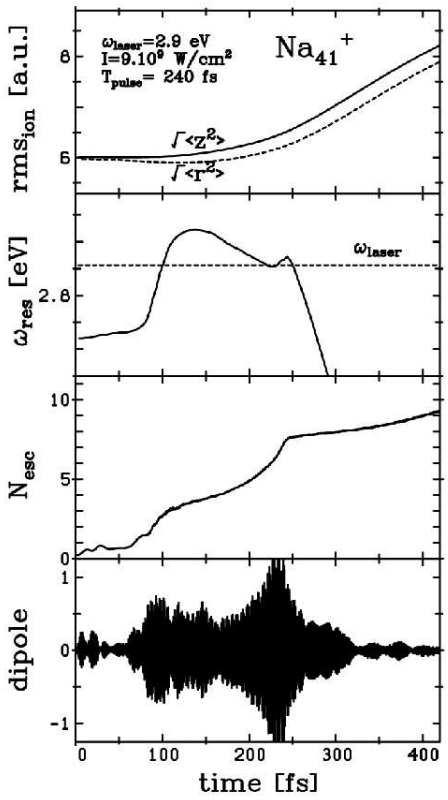

FIG. 16: TDLDA simulation of the excitation of Na_{41}^{+} with a laser of frequency $\omega = 2.86$ eV, intensity $I = 9 \times 10^9$ Wcm^{-2} and pulse length 240 fs. From top to bottom: global extension of the ionic distribution in the z direction (along laser polarization) and axial r direction (transverse to laser polarization), average resonance frequency for the actual structure and charge state, number of emitted electrons N_{esc} and dipole signal. Reproduced from Ref. [125] with permission of World Scientific.

C. High harmonic generation

By irradiating an atom, a molecule or a surface with a high intensity laser, an electron may absorb several photons and then return to its original state by emitting a single photon. The emitted photon will have a frequency that is a multiple number of the laser frequency. This process is known as high harmonic generation. Since the emitted high energy photons maintain a high coherence, they can be used as a source for X ray lasers. Fig. 17 shows the experimental[126] and calculated harmonic spectrum of the Helium atom. The solid line gives the theoretical results[127] obtained from the TDDFT using the EXX functional. The spectrum shows a series of peaks that first decrease in amplitude, until a plateau is reached that extends to very high frequency. The frequencies of the peaks are odd multiples of the laser frequency. The even multiples are dipole forbidden by symmetry. All theoretical approaches based on perturbation theory would produce a harmonic spectrum that decays exponentially. TDDFT, on the other hand, reproduces well the measured intensities

Another important process in high harmonic generation from molecules is the nuclear motion. Even harmonics may be created by irradiating HD with an intense laser pulse, but not by irradiating H_2: even harmonic generation is forbidden for a centrosymmetric molecule. In an adiabatic treatment of the nuclear coordinates, the nuclear masses play no role and the even harmonics do not appear. This is no longer the case if non-adiabatic effects are taken into account, for the different masses of H and D break the symmetry. Kreibich et al.[128] studied this process in a 1D model with a full quantum me-

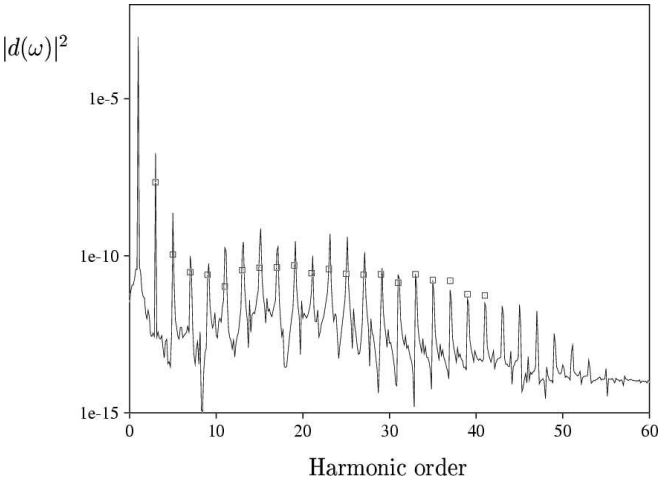

FIG. 17: Calculated harmonic spectrum of He irradiated at a wavelength of 616 nm and intensity of 3.5×10^{14} W/cm^2. The squares represent the experimental data,[126] normalized to the value of the 33rd harmonic of the calculated spectrum. Reproduced from Ref. [127] with permission of Kluwer.

chanical treatment of the nuclear motion, finding strong even harmonics at high harmonic number. To discern whether the classical treatment of nuclear motion also produces these harmonics, we have studied the same 1D problem within our framework, using in this case the EXX potential. The spectral intensity of the generated harmonics, $H(\omega)$, was calculated from the expression:

$$H(\omega) \sim \left| \int \mathrm{d}t\, \mathrm{e}^{\mathrm{i}\omega t} \frac{\mathrm{d}^2}{\mathrm{d}t^2} \langle \Psi(t) | \hat{e} \cdot \mathbf{D}(t) | \Psi(t) \rangle \right|^2 . \qquad (3.1)$$

where $\hat{e}$ is the polarization vector, $\Psi(t)$ the Kohn-Sham wavefunction and $\mathbf{D}(t)$ is the time evolution of the dipole moment of the molecule. The laser pulse frequency was 770 nm, and its total length 30 cycles. The shape was a linear ramp until the 10th cycle, and constant thereafter.

We find that the classical treatment does indeed produce even harmonics, but much smaller than the quantum treatment. The results are shown in Fig. 18. The top left panel shows the harmonic spectrum for HD, and only odd harmonics are apparent. However, one can prove that the Hamiltonian of the HD molecule already violates centrosymmetry within our classical treatment, through a term of the form:

$$-\frac{1}{2}\left(\frac{1}{M_H} - \frac{1}{M_D}\right) P(t)\,[\hat{p}_1 + \hat{p}_2]\,, \qquad (3.2)$$

where $P(t) = \frac{1}{2}(P_H(t) - P_D(t))$ is the relative time-dependent nuclear momentum and $\hat{p}_i$ are the electronic momentum operators. Its effect can be enhanced by decreasing the nuclear masses. In the bottom left panel, the H and D masses have been decreased by a factor 100, and then the second- and fourth-order harmonics become visible. As a qualitative check of the numerics, we also show the same graphs for H_2, in which no even harmonics can occur. Thus we see that on a qualitative level the non-adiabatic dynamics generating even harmonics is obtained with the classical treatment of the nuclear coordinates. However, the quantum treatment may be needed for a quantitative result. By describing the nuclei quantum mechanically, the ground state violates centrosymmetry and the even harmonics can be generated. In contrast, in the classical treatment the electronic ground state is symmetric and the symmetry violation only builds up as the nuclei move.

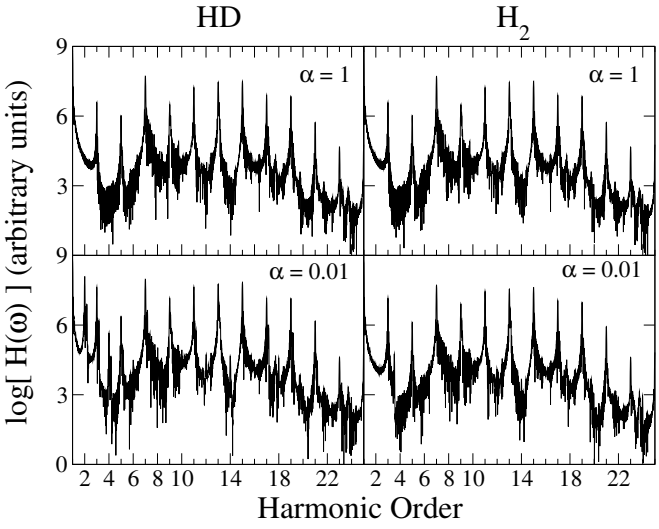

FIG. 18: Harmonic spectra of HD (left panels) and H_2 (right panels). The nuclear masses used in the calculation are $m' = \alpha m$, being m the real mass. In this way, top plots are made using for the nuclear masses their real values whereas bottom plots are made using a hundredth of their real values. Reproduced from Ref. [35] with permission of EDP Sciences.

IV. CONCLUSIONS AND PERSPECTIVES

Most characterization tools in physics, chemistry and biology as well as electro/optical devices are based on the understanding of the interaction of photons and electrons with matter. Moreover, many fundamental questions concerning the theoretical and numerical descriptions of this interaction are still open. In the present work we focus on one technique to describe electronic excitations in finite and extended systems, namely, time-dependent density functional theory.[129] Some points have been treated more in detail than others. However our goal has been to give a glimpse on the potential of TDDFT, the open questions and future lines of development.

The first applications of TDDFT[17] (which were presented years before the theory was mathematically well founded[1]) dealt with processes within the linear regime, where the electromagnetic field that probes the matter under study may be regarded as a small perturbation to the internal fields. For this kind of calculations (i.e. photoabsorption cross section of organic- and bio-molecules and nanostructures, excitation energies, circular dichroism, etc.), TDDFT has become almost a standard, and competes with increasing success with more expensive quantum-chemistry-like and many-body-perturbation theory approaches.[4] In this review we presented some examples for rather different systems: from atoms to middle sized protein chromophores; from metallic clusters to organic molecules. Most of the results were obtained solving the time-dependent Kohn-Sham equations directly in the time domain. However, for completenss we have sketched the standard application in the frequency domain.[2–4] The good scalability of the time-propagation methodology with system-size permits to forecast successful calculations of large biomolecular systems as for example retinal, the optical absorption of the green fluorescent protein, presented here, being already one first example. Non surprisingly, the study of processes of biological interest by means of TDDFT is currently a hot research topic. For this purpose, one of the challenges to be achieved is the inclusion of environment effects in the treatment of the response to external fields of nanostructures and biostructures. In spite of the wide variety of systems that may be handled by the ab-initio TDDFT approach, the description of a full protein is still beyond its scope. In this context, the objectives are both a proper separation of a chemically active region from an almost-inert environment, as in standard QM-MM techniques,[106–108] and a proper recipe to consider their mutual interaction (see for example Ref. [130] for some re-

cent work along the perturbative treatment of solvent effects in the response function of molecules in solution).

If we increase the size of the system towards a periodic structure in one, two and three dimensions (i.e. polymers, slabs, surfaces or solids), we must be careful with the form of the functional and the treatment of external electric and magnetic fields. Difficulties arise, for example, in long conjugated molecular chains, where the strong non-locality of the exact functional is not well reproduced in the usual approximations. A related problem appears for semiconductors: the exchange and correlation kernel f_{xc} should behave asymptotically, in momentum space, as $1/q^2$ when $q \to 0$,[4,46] which is not the case for the adiabatic LDA or GGA, so succesful for small finite systems. Moreover, the technical details related to the implementation of a time-propagation scheme for obtaining the electrical response of solids has already been solved,[131] and efforts are under way[132] to obtain a proper treatment of periodic structures in one and two-dimensions (like infinite chains and slabs). In any case, input from more accurate many-body theories is needed to improve the exchange-correlation functionals to be used within the TDDFT scheme.[4]

Succesful as it may be in the linear regime, one of the main strengths of the TDDFT theory is, however, its ability to cope with nonlinear processes. The interest in these processes has grown in recent years, partly due to the increasing availability of high-intensity ($> 10^{15}$ W/cm^2) and short duration (< 1 fs) sources of laser radiation. The interaction of these fields with matter leads to a variety of new phenomena: above-threshold dissociation or ionization, very-high harmonic generation, bond softening, etc. The possibility of monitoring, controlling or triggering chemical reactions by means of properly tailored laser pulses is especially appealing; some ground-breaking experimental advances oriented to this purpose have been reported in the past few years. By definition, perturbative approaches are in principle unsuitable for the simulation of these phenomena since the applied fields are of the order of, or even larger than the molecular fields. It is clear then that TDDFT has an application niche here. We have also presented some examples of the applications of TDDFT to this area: cluster fission, molecular photo-dissociation in strong laser fields or generation of high harmonics. Another relevant application concerns the characterisation and visualisation of the formation of chemical bonds in a chemical reaction or by the interaction with an external electromagnetic field.[133]

Density functional theory and its time-dependent extension are successful because of their computational advantages compared to quantum-chemistry methodologies. An enormous amount of effort is being put onto the subject by many research groups. In this review, we have by no means tried to describe all the numerous approaches and applications; on the contrary, the majority of the calculations presented here have been performed with our home-grown `octopus` project. This platform attempts to sustain a useful tool for the applications of TDDFT. However, the optimal implementation of the necessary equations in a computational scheme is far from being simple. The research on this field must be consequent with a twofold orientation: the main objective, which is of course the investigation of a wide variety of physical phenomena, as manifested in the preceding sections; second, the numerical investigations pursuing the most practical algorithms.

In spite of its success, TDDFT has a number of commonly invoked failures. One example is the above-mentioned difficulty encountered when studying extended systems; another one is the severe underestimation of high-lying excitation energies in molecules when simple exchange and correlation functionals are employed. These failures, however, must be well understood: TDDFT is an exact reformulation of the time-dependent Schrödinger equation and, in consequence, all those properties of physical systems coupled to external electromagnetic fields (either in the linear, or in the non linear regime) that are properly described by Quantum Theory must also be attainable by means of the *exact* TDDFT. Unfortunately, one of the objects that conform the TDDFT equations, the exchange and correlation potential, has to be approximated. The failures that are commonly adscribed to TDDFT should in fact be imputed to the functionals in use. One of the usual criticisms cast over DFT, the absence of a well defined and systematic procedure to improve the quality of the functionals, may well be extended to the time-dependent version of the theory. However, the advances in the investigation of functionals during the last years, have broaden the field of applicability of the theory, as demonstrated by the variety of examples presented in this review.

Acknowledgements

This work was supported by the EC Research Training Networks NANOPHASE (HPRN-CT-2000-00167), COMELCAN (HPRN-CT-2000-00128), and EXCITING (HPRN-CT-2002-00317), by Spanish MCyT (Grants MAT2001-0946 and MAT2002-04499-C02-01), Junta de Castilla y Leon (Grant CO 01-102) and by the University of the Basque Country (9/UPV 00206.215-13639/2001). Computer time was granted by CEPBA (Barcelona), CFC (Coimbra), and DIPC. Three of us, AC, MALM and JAA, also thank the DIPC for hospitality and support. We benefited from stimulating discussions and collaborations with G. F. Bertsch, M. L. Cohen, R. Del Sole, P. M. Echenique, R. Godby, E. K. U. Gross, X. López, S. G. Louie, A. Marini, Y. Miyamoto, G. Onida, L. Reining, D. Tomanek, D. Varsano, L. Wirtz and K. Yabana.

* alberto.castro@tddft.org
† marques@tddft.org
‡ jaalonso@fta.uva.es
§ arubio@sc.ehu.es

[1] M. A. L. Marques and E. K. U. Gross, in A Primer in Density Functional Theory, C. Fiolhais, F. Nogueira and M. Marques

(Editors), Lecture Notes in Physics 620, Springer Verlag, Berlin (2003), p. 144.
[2] E. K. U. Gross, J. Dobson, and M. Petersilka, in Density Functional Theory II, R. F. Nalewajski (Editor), Topics in Current Chemistry 181, Springer Verlag, Berlin (1986), p. 81.
[3] R. van Leeuwen, Int. J. Mod. Phys. B 15, 1969 (2001); K. Burke, M. Petersilka and E. K. U. Gross, in Recent Advances in Density Functional Methods, P. Fantucci and A. Bencini (Editors), World Scientific, Singapore (2002), p. 67.
[4] G. Onida, L. Reinig and A. Rubio, Rev. Mod. Phys. 74, 601 (2002).
[5] M. A. L. Marques, A. Castro, G. F. Bertsch and A. Rubio, Computer Phys. Commun. 151, 60 (2003). The `octopus code` is available at http://www.tddft.org/programs/octopus.
[6] M. Brack, Rev. Mod. Phys. 65, 677 (1993); M. Brack, Phys. Rev. B 39, 3533 (1989); O. Bohigas, A. M. Lane and J. Martorell, Phys. Reports 51, 267 (1979).
[7] C. R. C. Wang, S. Pollack, D. Cameron and M. M. Kappes, J. Chem. Phys. 93, 3787 (1990); K. Selby, M. Vollmer, J. Masui, V. Kresin, W. A. de Heer and W. D. Knight, Phys. Rev. B 40, 5417 (1989).
[8] W. A. de Heer, K. Selby, V. Kresin, J. Masui, M. Vollmer, A. Chatelain and W. D., Knight, Phys. Rev. Lett. 59, 1805 (1987).
[9] G. F. Bertsch and R. A. Broglia, Oscillations in Finite Quantum Systems, Cambridge University Press, Cambridge (1994).
[10] D. Bohm and D. Pines, Phys. Rev. 92, 609 (1953).
[11] W. A. de Heer, Rev. Mod. Phys. 65, 611 (1993).
[12] In this model, the positive charge background of the ions is smeared out over the volume of the cluster, to form a distribution of positive charge with density $n_+(\mathbf{r}) = n_+^0 \Theta(R-r)$, where $\Theta(R-r)$ is the step function, with values 1 for $r < R$ and 0 for $r > R$. The radius R of the positive background is related to the number of atoms N in the cluster by $\frac{4}{3}\pi R^3 = N\Omega$ where Ω is the experimental volume per atom in the bulk metal. Also, the constant n_+^0 is related to Ω and to the valence Z ($Z = 1$ for alkali elements) by $Z = n_+^0 \Omega$.
[13] G. Mie, Ann. Phys. (Leipzig) 25, 377 (1908).
[14] Ll. Serra, F. Garcías, N. Barberán, M. Barranco, J. Navarro and A. Rubio, Z. Phys. D 19, 89 (1991); Ll. Serra, F. Garcías, M. Barranco, J. Navarro, L. C. Balbás, A. Rubio and A. Mañanes, J. Phys.: Cond. Matter 1, 10391 (1989).
[15] P. Hohenberg and W. Kohn, Phys. Rev. 136, B864 (1964); W. Kohn and L. J. Sham. Phys. Rev. 140, A1133 (1965).
[16] R. M. Dreizler and E. K. U. Gross, Density Functional Theory. An Approach to the Quantum Many Body Problem, Springer-Verlag, Berlin (1990); R. G. Parr and W. Yang, Density Functional Theory of Atoms and Molecules, Oxford University Press, Oxford (1989); S. Lundqvist and N. H. March (Editors), Theory of the Inhomogeneous Electron Gas, Plenum Press, New York (1983).
[17] M. J. Stott and E. Zaremba, Phys. Rev. A 21, 12 (1980); A. Zangwill and P. Soven, Phys. Rev. A 21, 1561 (1980).
[18] E. Runge and E. K. U. Gross, Phys. Rev. Lett. 52, 997 (1984).
[19] R. van Leeuwen Phys. Rev. Lett. 80, 1280 (1998).
[20] C. O. Almbladh, and U. von Barth, Phys. Rev. B 31, 3231 (1985).
[21] J. P. Perdew and M. Levy, Phys. Rev. B 56, 16021 (1997).
[22] D. P. Chong, O. V. Gritsenko and E. J. Baerends, J. Chem. Phys. 116, 1760 (2002).
[23] R. O. Jones and O. Gunnarsson, Rev. Mod. Phys. 61, 689 (1989).
[24] M. Petersilka, U. J. Gossmann and E. K. U. Gross, Phys. Rev. Lett. 76, 1212 (1996); M. Petersilka and E.K.U. Gross, Int. J. Quantum Chem. 30, 181 (1996).
[25] A. L. Fetter and J. D. Walecka, Quantum Theory of Many-Body Systems, Mc Graw Hill, New York (1971).
[26] M. Casida, in Recent Developments and Applications in Density Functional Theory, J. Seminario (Editor), Elsevier, Amsterdam (1996), p. 391.
[27] I. Vasiliev, S. Ögut and J. R. Chelikowsky, Phys. Rev. Lett. 82, 1919 (1999), and references therein.
[28] I. Vasiliev, S. Ögut and J. R. Chelikowsky, Phys. Rev. B. 65, 115416 (2002).
[29] The transition-space representation is based on similarities with the time-dependent Hartree-Fock approach.[30]
[30] P.W. Langhoff, S.T. Epstein and M. Karplus, Rev. Mod. Phys. 44, 602 (1972).
[31] H. Flocard, S. E. Koonin and M. S. Weiss, Phys. Rev. C 17, 1682 (1978).
[32] K. Yabana and G. F. Bertsch, Phys. Rev. B 54, 4484 (1996); Z. Phys. D 42, 219 (1997); Phys. Rev. A 58, 2604 (1999); Phys. Rev. A 60, 1271 (1999).
[33] K. Yabana and G. F. Bertsch, Phys. Rev. A 60, 1273 (1999).
[34] M. A. L. Marques, A. Castro and A. Rubio, J. Chem. Phys. 115, 3006 (2001).
[35] A. Castro, M. A. L. Marques, J. A. Alonso, G. F. Bertsch, K. Yabana and A. Rubio, J. Chem. Phys. 116, 1930 (2002).
[36] A. Castro, M.A.L. Marques, J.A Alonso, G.F. Bertsch, and A. Rubio, Eur. J. Phys. D 28 211 (2004).
[37] M.A.L Marques, X. López, D. Varsano, A. Castro, and A. Rubio, Phys. Rev. Lett. 90, 258101 (2003).
[38] D. Varsano, A. Castro, M.A.L. Marques, and A. Rubio (work in progress).
[39] M. di Ventra and S. Pantelides, Phys. Rev. B 61, 16207 (2000); M. di Ventra, S. Pantelides and N. Lang, Phys. Rev. Lett. 88, 046801 (2002).
[40] E. U. K. Gross and W. Kohn, Adv. Quantum Chem. 21, 255 (1990).
[41] Richardson and Ashcroft [C.F. Richardson and N. W. Ashcroft, Phys. Rev. B 50, 8170 (1994)] proposed a dynamical parameterization of the kernel based on a summation of self-energy and fluctuation terms in the diagrammatic expansion of the polarization function for the homogeneous electron gas. It is constructed to satisfy many known exact conditions (static and dynamic). This parameterization is assumed to be very close to the exact dynamical exchange-correlation kernel. For a corrected parameterization see: M. Lein, E.K.U. Gross and J.P. Perdew, Phys. Rev. B 61, 13431 (2000).
[42] Y. H. Kim and A. Görling, Phys. Rev. Lett. 89, 096402 (2002); Phys. Rev. B 66, 035114 (2002).
[43] S. Kurth and U. Von Barth (unpublished).
[44] J. B. Krieger, Y. Li and G. J. Iafrate, Phys. Rev. A 45, 101 (1992).
[45] C. A. Ullrich, U. Gossmann and E. K. U. Gross, Phys. Rev. Lett. 74, 872 (1995).
[46] L. Reining, V. Olevano, A. Rubio, and G. Onida, Phys. Rev. Lett. 88, 066404 (2002).
[47] F. Sottile, V. Olevano and L. Reining, Phys. Rev. Lett. 91, 05640 (2003).
[48] A. Marini, R. Del Sole and A. Rubio, Phys. Rev. Lett. 91, 256402 (2003).
[49] J. P. Perdew, K. Burke and M. Ernzerhof, Phys. Rev. Lett. 77, 3865 (1996).
[50] R. Van Leeuwen and E. J. Baerends, Phys. Rev. A 49, 2421 (1994).
[51] M. E. Casida and D. R. Salahub, J. Chem. Phys. 113, 8918 (2000).
[52] J. P. Perdew and A. Zunger, Phys. Rev. B 23, 5408 (1981).
[53] G. Onida, L. Reinig, R. W. Godby, R. Del Sole and W. Andreoni, Phys. Rev. Lett. 75, 818 (1995).

[54] The GW corrections to the energies of the empty states are between 0.75 and 0.9 eV. The HOMO and the lowest occupied state are lowered by 1.55 and 1.4 eV, respectively. This leads to a HOMO-LUMO gap of 3.0 eV, to be compared to the small LDA gap of 0.55 eV. These large corrections are expected for a system in which screening is weak. The calculation of Onida et al.[53] also includes excitonic effects.

[55] J. G. Grossman, M. Rohlfing, L. Mitas, S. G. Louie and M. L. Cohen, Phys. Rev. Lett. 86, 472 (2001).

[56] U. Itoh, Y. Toyoshima, H. Onuki, N. Washida and T. Ibuki, J. Chem. Phys. 85, 4867 (1986).

[57] C. E. Moore, Nat. Stand. Ref. Data Ser. (U.S. Nat. Bur. Stand.) 35, Vol. I-III (1971).

[58] E. K. U. Gross, T. Kreibig, M. Lein and M. Petersilka, in Electron Correlations and Material Properties, A. Gonis, N. Kioussis and M. Ciftan (Editors), Plenum Press, New York (1999), p. 393.

[59] S. J. A. Van Gisbergen, F. Kootstra, P. R. T. Schipper, O. V. Gritsenko, J. G. Snijders and E. J. Baerends, Phys. Rev. A 57, 2556 (1998).

[60] A. Castro, PhD. Dissertation, University of Valladolid (2004),

[61] A. Rubio, J. A. Alonso, X. Blase, L. C. Balbás and S. G. Louie, Phys. Rev. Lett. 77, 247 (1996); (Erratum 77, 5442 (1996)). The calculated value of the polarizability of Li_8 given in this paper is not correct. The corrected value is 97.

[62] A. Rubio, J. A. Alonso, X. Blase and S. G. Louie, Int. J. Mod. Phys. B 11, 2727 (1997).

[63] J. Blanc, V. Bonacic-Koutecky, M. Broyer, J. Chevaleyre, Ph. Dugourd, J. Koutecky, C. Scheuch, J. P. Wolf and L. J. Wöste, Chem. Phys. 96, 1793 (1992).

[64] C. R. C. Wang, S. Pollack, D. Cameron and M. M. Kappes, Chem. Phys. Lett. 165, 26 (1990).

[65] V. Bonacic Koutecky, J. Pittner, C. Fuchs, P. Fantucci and J. Koutecky, J. Chem. Phys. 104, 1427 (1996).

[66] The calculated photoabsorption cross section of Na_8 gives similar results:[61] a plasmon peak at 2.55 eV to be compared with the experimental value of 2.53 eV.[7]

[67] S. Pollack, C. R. C. Wang, T. A. Dahlsheid and M. M. Kappes, J. Chem. Phys. 96, 4918 (1992).

[68] V. Bonacic-Koutecky, J. Gaus, M. Guest and J. Koutecky, J. Chem. Phys. 96, 4934 (1992).

[69] T. A. Dahlseid, M. M. Kappes, J. A. Pople and J. Ratner, J. Chem. Phys. 96, 4924 (1992).

[70] M. D. Deshpande, D. G. Kanhere, P. V. Panat, I. Vasiliev and R. M. Martin, Phys. Rev. A65, 053204 (2002).

[71] H. Häkkinen, M. Moseler and U. Landman, Phys. Rev. Lett. 89, 033401 (2002), and references therein.

[72] Ll. Serra and A. Rubio, Phys. Rev. Lett. 78, 1428 (1997); Z. Phys. D 40, 262 (1993); K. Yabana and G.F. Bertsch, Phys. Rev. A 60, 3809 (1999).

[73] J. Tiggesbäumker, L. Köller, and K. H. Meiwes-Broer, Chem. Phys. Lett. 260, 428 (1996); J. Tiggesbäumker, L. Köller, K. H. Meiwes-Broer, and A. Liebsch, Phys. Rev. A 48, R1749 (1993).

[74] E. Cottancin, J. Lerme, M. Gaudry, M. Pellarin, J.L. Vialle, M. Broyer, B. Prevel, M. Trilleus and P. Mélinon, Phys. Rev. B 62, 5179 (2000), and refernces therein.

[75] A. Sanchez, S. Abbet, U. Heiz, W. D. Schneider, H. Häkkinen, R.N. Barnett, and U. Landman, J. Phys. Chem. A 103, 9573 (1999)

[76] A. Romero, A. Castro, M.A.L. Marques and A. Rubio (unpublished).

[77] U. Näher, S. Bjornholm, S. Frauendorf, F. Garcias and C. Guet, Phys. Rep. 285, 245 (1997).

[78] J. A. Alonso, M. Barranco, F. Garcias, P. G. Reinhard and E. Suraud, E., in Fission Dynamics of Atomic Clusters and Nuclei, J. da Providencia, D. M. Brink, F. Karpechine and F. B. Malik (Editors), World Scientific, Singapore (2001), p. 163.

[79] H. Tee, V. A. Lobastov, U. M. Gomez, B. M. Godson, R. Srinivasan, C. Y. Ruan and A. H. Zewail, Science 291, 458 (2001).

[80] V. S. Sundström (Editor), Femtosecond chemistry and femtobiology: ultrafast reaction dynamics of atomic scale resolution, Nobel Symposium 101, Imperial College Press, London (1996).

[81] C. Yannouleas, R. A. Broglia, M. Brack and P. F. Bortignon, Phys. Rev. Lett. 63, 255 (1989); W. Ekardt and Z. Penzar, Phys. Rev. B 43, 1322 (1991).

[82] Z. Penzar, W. Ekardt and A. Rubio, Phys. Rev. B 42, 5040 (1990).

[83] J. M. Pacheco and W. D. Schöne, Phys. Rev. Lett. 79, 4986 (1997).

[84] M. Moseler, H. Häkkinen and U. Landman, Phys. Rev. Lett. 87, 053401 (2001).

[85] M. Schmidt, C. Ellert, W. Kronmüller and H. Haberland, Phys. Rev. B 59, 10970 (1999).

[86] D.L. Lichtenberger, M.E. Jatcko, K.W. Nebesny, C.D. Ray, D.R. Huffman and L.D. Lamb, Chem. Phys. Lett. 176, 203 (1991); J.H. Weaver, J.L. Martins, T. Komeda, Y. Chen, T.R. Ohno, G.H. Kroll and N. Troullier, Phys. Rev. Lett. 66, 1741 (1991).

[87] A. Rubio, J. A. Alonso, J. M. López and M. J. Stott, Physica B 183, 247 (1993).

[88] A.G. Marinopoulos, L. Reining, V. Olevano, A. Rubio, T. Pichler, X. Liu, M. Knupfer and J. Fink , Phys. Rev. Lett. 89, 076402 (2002); and references therein.

[89] H. Ajie, M.M. Alvarez, S.J. Anz, R.D. Beck, F. Diederich, K. Fostiropoulos, D.R. Huffman, W. Krätschmer, Y. Rubin, K.E. Schriver, D. Sensharma and R.L. Whetten, J. Phys. Chem. 94, 8630 (1990).

[90] I.V. Hertel, H. Steger, J. de Vries, B. Weisser, C. Menzel, B. Kamke and W. Kamke, Phys. Rev. Lett. 68, 784 (1992).

[91] N. S. Goroff, Acc. Chem. Res. 29, 77 (1996).

[92] H. Prinzbach, A. Weiler, P. Landenberger, F. Wahl, J. Wörth, L. T. Scott, M. Gelmont, D. Olevano and B. Von Issendorff, Nature 407, 60 (2000).

[93] J. C. Grossmann, L. Mitas and K. Raghavachari, Phys. Rev. Lett. 75, 3870 (1995).

[94] R. O. Jones and G. Seifert, Phys. Rev. Lett. 79, 443 (1997).

[95] K. Raghavachari, D. L. Strout, G. K. Odom, G. E. Scuseria, J. A. Pople, B. G. Johnson and P. M. W. Gill, Chem. Phys. Lett. 214, 357 (1992).

[96] E. J. Bylaska, P. R. Taylor, R. Kawai and J. H. Weare, J. Phys. Chem. 100, 6966 (1996).

[97] J. M. Pacheco and J. L. Martins, J. Chem. Phys. 106, 6039 (1997).

[98] J. Lu, S. Re, Y, Choe, S. Nagase, Y. Zhou, R. Han, L. Peng, X. Zhang and X. Zhao, Phys. Rev. B 67, 125415 (2003).

[99] A. J. Stone and D. J. Wales, Chem. Phys. Lett. 28, 501 (1986).

[100] R. O. Jones, J. Chem. Phys. 110, 5189 (1999).

[101] M. E. Casida, C. Jamorski, K. C. Casida and D. R. Salahub, J. Chem. Phys. 108, 4439 (1998).

[102] S. Grimme and M. Parac, Phys. Chem. Chem. Phys. 3, 292 (2003).

[103] E. E. Koch and A. Otto, Chem. Phys. Lett. 12, 476 (1972).

[104] T. M. H. Creemers, A. J. Lock, V. Subramaniam, T. M. Jovin, and S. Völker, Proc. Natl. Acad. Sci. U.S.A. 97, 2974 (2000); Nat. Struct. Biol. 6, 557 (1999).

[105] S. B. Nielsen, A. Lapierre, J. U. Andersen, U. V. Pedersen, S. Tomita and L. H. Andersen, Phys. Rev. Lett. 87, 228102 (2001).

[106] B. R. Brooks, R. E. Bruccoleri, B. D. Olafson, D. J. States, S. Swaminathan and M. Karplus, J. Comput. Chem. 2, 187 (1983).

[107] M. J. Field and P.A. Bash and M. Karplus, J. Comp. Chem. 11,

700 (1990).
[108] J. Gao, in Methods and applications of combined quantum mechanical and molecular mechanics potentials, Reviews in Computational Chemistry 7, VCH, New York (1995), p. 119.
[109] M. J. S. Dewar and E. Zoebisch and E. F. Healy and J.J.P. Stewart, J. Am. Chem. Soc. 107, 3902 (1995).
[110] T. Brabec and F. Krausz, Rev. Mod. Phys. 72, 545 (2000).
[111] M. Protopapas, C. H. Keitel and P. L. Knight, Rep. Progr. Phys. 60, 389 (1997).
[112] A. González-Ureña, K. Gasmin, A. Rubio and P.M. Echenique, Eur. Phys. J. D 28, 193 (2004).
[113] V. Stert, H. H. Ritze, P. Farmanara and W. Radloff, Phys. Chem. Chem. Phys. 3, 3939 (2001), and references therein.
[114] M. Rosi and C. W. Bauschlicher Jr., Chem. Phys. Lett. 159, 479 (1989); V. Staemmler, Z. Phys. D 22, 741 (1992); F. X. Gadea and I. Paidarová, Chem. Phys. 209, 281 (1996).
[115] H. Haberland, B. v. Issendorff, R. Fröchtenicht and J. P. Toennies, J. Chem. Phys. 102, 8773 (1995).
[116] J. A. Gascón, Electronic and Structural Properties of Rare Gas Cation Clusters, PhD Dissertation (2002), and references therein.
[117] H. Haberland, A. Holfmann and B. v. Issendorff, J. Chem. Phys. 103, 3450 (1995).
[118] H. Hohmann, C. Callegari, S. Furrer, D. Grosenick, E. E. B. Campbell and I. V. Hertel, Phys. Rev. Lett. 73, 1919 (1994).
[119] R. Schlipper, R. Kusche, B. von Issendorff and H. Haberland, Phys. Rev. Lett. 80, 1194 (1998).
[120] M. Lezius, S. Dobosz, D. Normand, and M. Schmidt, Phys. Rev. Lett. 80, 261 (1998).
[121] L. Köller, M. Schumacher, J. Köhn, S. Teuber, J. Tiggesbäumker and K. H. Meiwes-Broer, Phys. Rev. Lett. 82, 3783 (1999).
[122] F. Calvayrac, P. G. Reinhard, E. Suraud, and C. Ullrich, Phys. Rep. 337, 493 (2000).
[123] T. Baumert and G. Gerber, Adv. At. Mol. Opt. Phys. 35, 163 (1995).
[124] F. Chandezon, C. Guet, B. A. Huber, D. Jalabert, M. Maurel, E. Monnand, C. Ristori, and J. C. Rocco, Phys. Rev. Lett. 74, 3784 (1995).
[125] E. Suraud, and P. G. Reinhard, Phys. Rev. Lett. 85, 2296 (2000); C. A. Ullrich, P. G. Reinhard and E. Suraud, J. Phys. B. 30, 5043 (1997).
[126] K. Miyazaki and H. Sakai, J. Phys. B 25, L83 (1992).
[127] C. A. Ullrich, S. Erhard and E. K. U. Gross, in Super Intense Laser Atom Physics (SLAP IV), H. G. Muller and M. A. Fedorov (Editors), Kluwer, Amsterdam, (1996).
[128] T. Kreibich, M. Lein, V. Engel, and E. K. U. Gross, Phys. Rev. Lett. 87, 103901 (2001).
[129] For comparison of this technique to standard many-body and quantum chemistry approaches see the reviews in Refs. [1–4].
[130] L. Jensen, P. T. van Duijen and J.G. Sniders, J. Chem. Phys. 119, 3800 (2003).
[131] G. F. Bertsch, J.-I. Iwata, A. Rubio and K. Yabana, Phys. Rev. B 62, 7998 (2000).
[132] C. Rozzi, A. Castro, M. A. L. Marques, E. K. U. Gross and A. Rubio (to be published).
[133] T. Burnus, M. A. L. Marques and E.K.U Gross (to be published).